Drop impact close to the edge of an inclined substrate: Liquid sheet formation and break-up

S. Lejeune and T. Gilet*
Microfluidics Lab, Department of Aerospace and Mechanical Engineering, University of Liège, Liège, Belgium

Raindrop impacts on plant leaves are responsible for the dispersal of several crop diseases. In this experimental study, we propose a generic impact configuration that shares several qualitative features with more complex impacts on leaves. We investigate the formation and break-up of a liquid sheet upon impact of a drop close to the horizontal edge of an inclined substrate. The impact Weber number, the distance from the impact point to the edge, and the substrate inclination are systematically varied. We analyze their influence on the kinematics of both the liquid spreading on substrate and the liquid sheet beyond the edge, as well as on the subsequent statistics of droplet ejection (radius, speed, time of ejection).

I. INTRODUCTION

Raindrop impacts and subsequent fragmentation in droplets participate to a variety of natural phenomena [1], from the erosion of soil [2, 3] and buildings [4] to the dispersal of seeds [5], particles [6] and foliar pathogens [7, 8]. The latter has dramatic consequences on the agricultural output worldwide [9], as many major crops are susceptible to some rain-dispersed pathogens [7]. Optimized cultivar mixtures with specific foliar architecture [10–12] and forecast models [13] can help mitigating the propagation of crop diseases, and therefore the need for pesticides. Recent work [8, 14] highlighted a special raindrop impact configuration that is both frequent in a rainfall on a canopy and efficient at dispersing contaminated droplets from an infected leaf. In this configuration named *crescent-moon* impact, a raindrop impacts next to a contaminated liquid residue in the form of a sessile drop on the plant leaf. The splashing raindrop pushes the sessile drop [15] which then stretches into a liquid sheet. The sheet expands normally to the substrate, then it retracts and the line of contact between the sheet and the substrate shrinks to a point. The sheet fragments into a myriad of droplets that may land on and contaminate surrounding healthy leaves (Fig. 1a). The effect is as impressive when the sessile drop is close to the edge of the leaf (Fig. 1b).

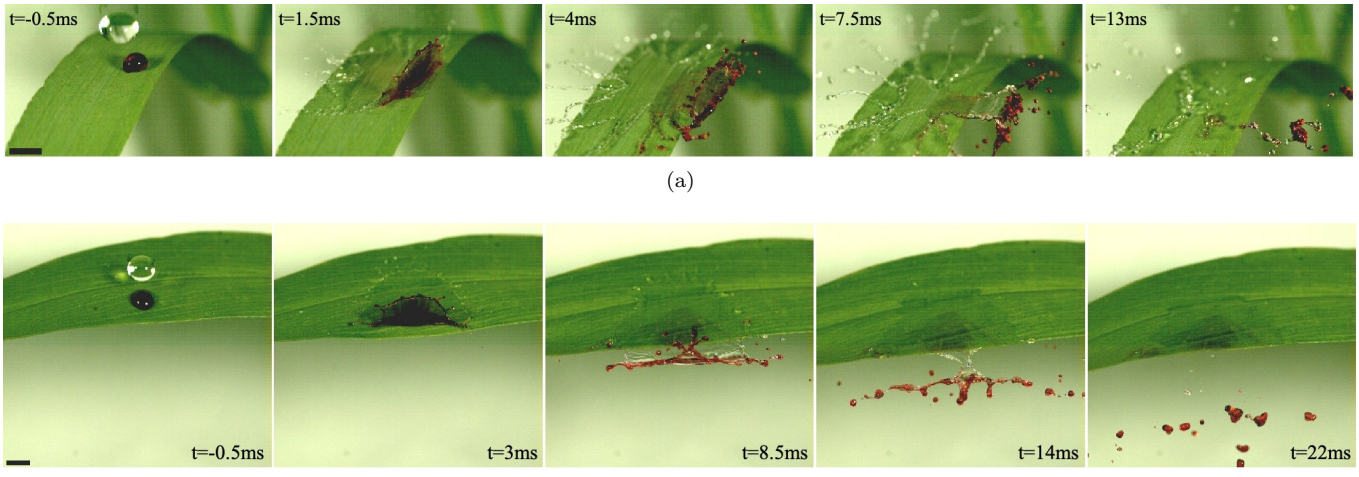

FIG. 1. (Color online) (a) *Crescent-moon* impact: a raindrop impacts next to and pushes a sessile drop of dyed water, which is then stretched in a liquid sheet and finally fragmented in droplets. The red dye represents potential pathogens that would be present in the contaminated liquid residue on the leaf. (b) *Crescent-moon* impact where the dyed, "contaminated" liquid sheet reaches the edge of the leaf. In both (a) and (b), the scale bar is 4 mm and the time t from impact is indicated on each snapshot [16].

* tristan.gilet@uliege.be

The dynamics of the liquid sheet may shape the distribution of mass and velocity of the ejected droplets [8]. However, the sheet developed in the *crescent-moon* impact configuration is strongly three-dimensional, so its kinematics is hard to image, quantify and rationalize. Nevertheless, the main ingredients of the *crescent-moon* impact can be found in the alternative configuration of a single drop impacting next to the straight edge of a horizontal substrate [17]. The spreading liquid reaches the edge and forms a liquid sheet in the air, still connected to the substrate. The sheet expands, then retracts mostly along the edge, separates, collapses and fragments in droplets. As most of these motions happen in the plane of the substrate, they are much easier to quantify. Both the sheet kinematics and subsequent droplet distributions were recently investigated in Lejeune *et al.* [17].

Previously, the formation of a liquid sheet beyond the edge of a substrate was mostly studied in the axisymmetric case of drop impacts on small circular horizontal posts [18–24]. It was recently extended to the non-axisymmetric cases of curved [25, 26] and partly inclined substrates [27]. The impact at speed V_0 of a drop of radius R_0 is mostly characterized by the dimensionless Weber number $We = 2\rho R_0 V_0^2/\sigma$, where ρ and σ are the density and surface tension of the liquid, respectively. This number represents a ratio of the kinetic and surface energy of the incoming drop. It is also proportional to the squared ratio of the capillary time $t_c = \sqrt{4\rho R_0^3/(3\sigma)}$ characteristic of drop oscillations and the impact time $t_i = 2R_0/V_0$ characteristic of the initial crushing of the drop upon impact. At $We \gg 1$, a drop impacting a horizontal pole forms an axisymmetric liquid sheet of thickness $h(r,t)$ surrounded by a toroidal liquid rim of major radius $R(t)$ and minor radius $b(t)$, where r is the radial coordinate. Villermaux and Bossa [20] proposed a model to predict $R(t)$ from the conservation of mass and momentum transferred from the sheet to the rim. This model is based on the hypothesis that $h/R_0 \sim R_0 t_i/(rt)$. Sheet thickness measurements [21, 23] showed that this hypothesis is only valid at times (from impact) much larger than t_i. Moreover, these measurements confirmed that fluid particles within the sheet do not accelerate until they reach the rim. Villermaux's model [20] shows that the sheet radius reaches a maximum of the order of $R_0 We^{1/2}$ in a time of the order of t_c. This scaling law was also observed for the normal extension of the sheet formed by drops impacting near straight edges [17]. The rim destabilizes owing to a combination of Rayleigh-Plateau and Rayleigh-Taylor instabilities [18, 20, 28] and ligaments originate from its corrugations, that later break-up into ejected droplets [20, 24]. The mean size of these droplets is proportional to the minor radius of the rim [20], which scales as $b \simeq \sqrt{\frac{\sigma}{-\rho\ddot{R}}} \simeq R_0 We^{-1/4}$, where $\ddot{R} = \mathrm{d}^2R/\mathrm{d}t^2$ [28].

Raindrop impacts on real plant leaves involve two additional ingredients: the leaf inclination [29] and its oscillation, the latter being induced both by the impact and possibly by additional wind [30, 31]. This motion of the substrate can quantitatively modify the outcome of the *crescent-moon* impact and strongly shape the dispersal pattern [8]. Besides absorbing some of the momentum and kinetic energy of the impacting raindrop [32, 33], the downward motion of a leaf stretches the liquid sheet of the *crescent-moon* impact even more [8], although it still remains three-dimensional [Fig. 2(a-b)]. The goal of this paper is to introduce a similar additional stretching of the liquid sheet in the two-dimensional configuration of a drop impacting next to the straight edge of a flat substrate. This is achieved by inclining the substrate downward while keeping the edge horizontal. The liquid sheet then remains approximately in the plane of the substrate, and it experiences additional stretching owing to the inherited tangential velocity of the impacting drop [Fig. 2(c)].

Drop impacts with some tangential velocity (either on inclined or laterally moving substrates) were mostly studied on hydrophobic surfaces, and often in a range of speed significantly smaller than that of raindrops [34–38]. Focus was made on transitions between different outcomes, including rebound [39] or prompt splash [40]. Laan *et al.* [41] reported an extensive investigation of the maximum spreading of a drop upon impact on horizontal and inclined substrates, within a wide range of impact speed. More recently, Almohammadi and Amirfazli [42] analyzed the spreading kinematics of drops impacting on a horizontal substrate translated horizontally at high speed. A quantitative kinematic analysis of drop spreading upon impact on inclined substrates is still missing.

The present paper is a first investigation of the formation and fragmentation of a liquid sheet originating from a drop impacting near the flat edge of an inclined substrate. The experimental setup is described in section II, then the general phenomenology is presented (section III). The motions of the spreading liquid on substrate, the expanding liquid sheet beyond the edge and the subsequently ejected droplets are quantified in sections IV, V and VI respectively. Their relation to each other as well as to the impact parameters is determined. The last section is a discussion and summary of the main results of this work.

II. EXPERIMENTAL SETUP

The experimental setup is similar to the one already described in Lejeune *et al.* [17]. Water drops drip from a certain height above an inclined substrate. The water is colored with a dye (Red Vahine from McCormick, Inc.) that does not significantly affect its physical properties (surface tension $\sigma \simeq 70$ mN/m, density $\rho \simeq 1000$ kg/m^3 and kinematic viscosity $\nu \simeq 10^{-6}$ m^2/s at room temperature 20 ± 2°C). The drops are formed at the tip of a plastic connector with

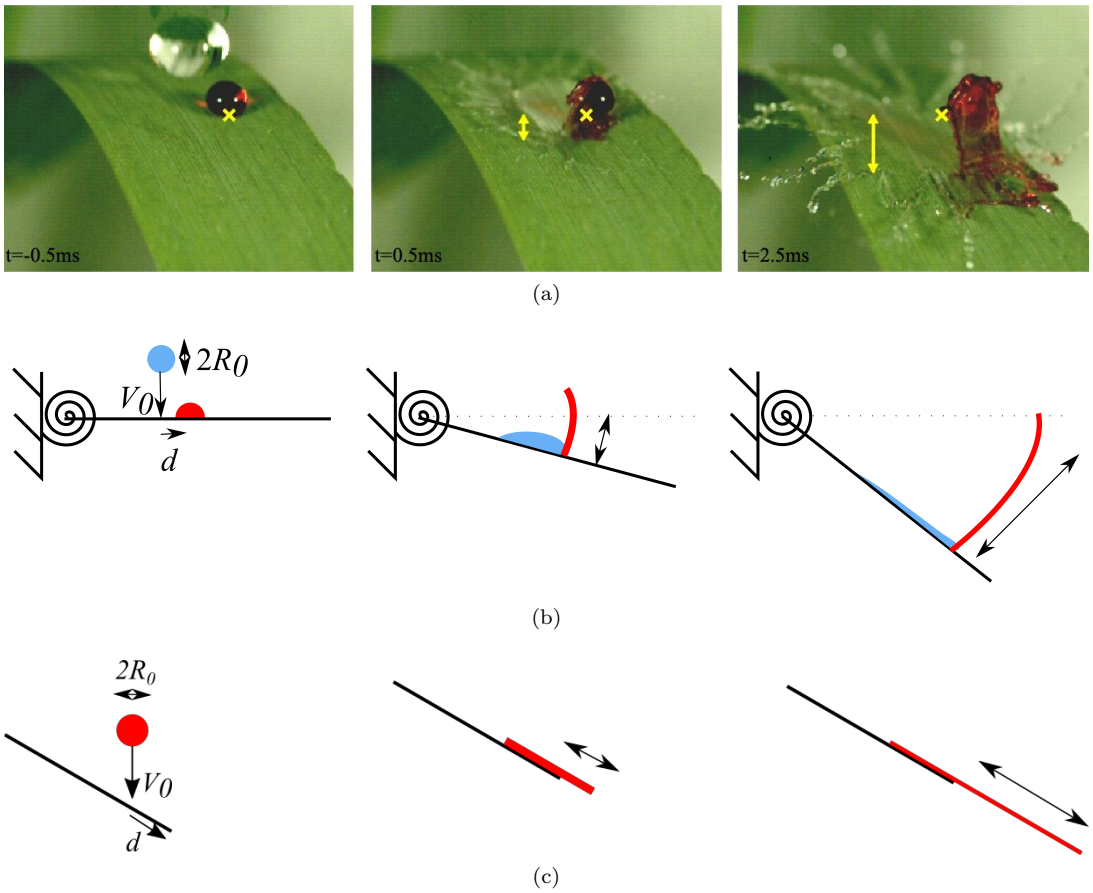

FIG. 2. (Color online)(a) A clear water drop impacts on a graminea leaf on which a dyed drop has been deposited. Upon impact, the leaf deflects downwards and stretches the liquid sheet. The time t from impact is indicated on each snapshot [16]. The yellow crosses and the double arrow indicate the original position of the leaf and the deflection from impact, respectively. (b) Schematic of the stretching of the *crescent-moon* liquid sheet due to the deflection of a leaf. The sheet is formed by the impact of a drop of radius R_0 and speed V_0 at a distance d from another sessile drop. (c) Schematic of the stretching of the liquid sheet following the impact of a single drop of radius R_0 and speed V_0 on an inclined substrate, at a distance d from its edge.

a constant flow rate imposed by a syringe pump (AL-1000 from WPI, Inc.). The drop radius $R_0 = 2.36 \pm 0.03$ mm is kept constant in the present experiments. Its value is inferred from a measurement of the drop mass with a precision balance (SE-VWRI611 from VWR, Inc.). The corresponding capillary time is $t_c \simeq 16$ ms.

These drops fall and impact near the straight edge of a flat substrate, inclined with an angle α from horizontal (positive downward), the edge being the axis of rotation. The substrate is made of dry plexiglass (XT from Superplastic, Inc., 2 mm thick) with advancing and receding contact angles for water of 85° and 55° (70° ± 15°), respectively. The average roughness of the edge is about 4 μm. The substrate is dried after each impact using a moist cloth to reduce the deposition of electrostatic charges. The offset d is defined as the distance between the impact point and the edge, counted positively when at least half the drop hits the substrate (Fig. 2c). It is varied with a millimeter stage (LT1 from Thorlabs, Inc.). The impact speed can be adjusted by changing the height of release above the substrate. Two different impact speeds $V_0 \in \{2.9 \pm 0.3, 5.6 \pm 0.1\}$ m/s were investigated, which correspond to impact times $t_i \in \{1.6, 0.8\}$ ms. An air shelter was placed to prevent major air currents from influencing the trajectory of the falling drop.

Two orthogonal views of the phenomenon are captured with synchronized high speed cameras and backlighting (Fig. 3). The first view (Photron Fastcam Mini UX, black and white, 4000 frames per second) is a side view of axis aligned with the edge. It allows accurate measurement of the impact speed V_0 and the offset d. It also serves to validate the assumption of a 2D liquid sheet in the plane of the substrate. Experiments at $d/R_0 < 1$ for which the sheet deviates from the plane of the substrate by more than 20° are excluded from the dataset [17]. The second view (Phantom MIRO 110, color, 2000 frames per second), referred as top view, is in fact normal to the substrate, looking downward, focused on the upper plane of the substrate in which most of the motion occurs (for the horizontal

substrate, the camera is slightly tilted in order not to obstruct the free fall of the impacting drop, and this is accounted for in the image processing). The kinematics of both the spreading liquid on solid, the liquid sheet in the air and the subsequent droplets can therefore be quantified from this second view. The resolution of both views (effective size of a pixel) is comprised between 56 μm and 100 μm and determined with an accuracy of 2 μm. Motion interpolation is achieved to determine accurately the time at which the drop impacts and the time at which the liquid reaches the edge of the substrate.

The variation of three main dimensionless numbers is considered in this paper: the inclination $\alpha \in [-40°, 60°]$, the dimensionless offset $d/R_0 \in [1, 16]$ and the Weber number $We \in \{565 \pm 20\%, 2115 \pm 4\%\}$. Since $We \gg 1$, inertia dominates the initial spreading of the drop and wetting properties are of lesser importance. This regime of We is within the range experienced by rainfalls [17]. Viscosity will not strongly affect the sheet kinematics, since the Ohnesorge number $Oh = \sqrt{\nu^2\rho/(2R_0\sigma)} \simeq 0.0017$ is much smaller than unity. Viscosity may nevertheless shape the break-up of small droplets ($\lesssim 20\mu$m), for which the corresponding Ohnesorge number would be around 0.025 [43, 44]. The influence of gravity on the liquid sheet kinematics is also negligible, as it will be proven in section V. Consequently, the regime investigated here is mostly dominated by the inertia and surface tension of the liquid.

III. PHENOMENOLOGY

An example of drop impact next to the edge of a substrate inclined downward by $\alpha = 60°$ is shown in Fig. 3. Immediately after impact [Fig. 3(a)], the drop spreads and reaches the edge of the substrate. The liquid then takes off and forms a liquid sheet surrounded by a thicker rim [Fig. 3(b)]. At such low We, capillary waves are emitted from the rim, both on the substrate and on the liquid sheet. While the drop keeps spreading, the rim advances synchronously on the solid side and on the air side of the edge. After maximum spreading, the rim on solid slightly recedes. By contrast, the rim on the air side of the edge now evolves independently and retracts completely. At the end of this retraction [Fig. 3(c)], both lateral rims on each side of the sheet collide with each other [Fig. 3(d)]. The collision here starts at the edge, then it propagates normally to the edge towards the sheet apex. This rim collision here generates a second, smaller liquid sheet mostly in the vertical plane perpendicular to the edge [visible in side view, Fig. 3(d-f)]. This latter, secondary sheet expands then collapses and may generate a third sheet, this time again in the plane of the substrate [slightly visible in top view of Fig. 3(f), but much better seen in the corresponding movie [16]]. The collapse of all these sheets forms ligaments that fragment into droplets [Fig. 3(f-g)]. This cascade of perpendicular liquid sheets formed by rim collisions is reminiscent of the fluid chains observed when two laminar jets collide [45, 46].

As the dimensionless offset d/R_0 is varied, three kinematic scenarios similar to those identified in Lejeune *et al.* [17] are observed (Fig. 4):

- (I) At large offset [Fig. 4(I)], the liquid has almost finished spreading when it reaches the edge. The spreading shape is very close to an ellipse that is continued by the liquid sheet beyond the edge [Fig. 4(Id)]. The sheet retraction is completed at the same time in both directions normal and tangent to the edge [Fig. 4(If)]. A marked difference induced by a downward inclination of the substrate is the presence of a thick rim that turns into a ligament then into large droplets [Fig. 4(If)]. Such ligament was already observed for the spreading upon impact of a blood drop on an inclined substrate [47].

- (II) At intermediate offset [Fig. 4(II)], the sheet expands in the air differently than on the substrate. The sheet retraction is again completed almost simultaneously along and normal to the edge, so the sheet remains connected to the edge at all time. The sheet collapses from its apex towards the edge [Fig. 4(IIe)]. The collision of opposite rims forms a secondary liquid sheet perpendicular to the substrate, whose breakup generates droplets that are significantly smaller than those possibly ejected from the rim of the first sheet.

- (III) At small offset [Fig. 4(III)], the sheet keeps moving away from the edge while it retracts along the edge. The rim collision occurs at the edge first, and it then propagates towards the sheet apex [Fig. 4(IIId)]. Consequently, this first sheet still exists when the secondary sheet is formed, and it keeps moving away, now fully separated from the edge. The collapse of this second, smaller sheet forms a third sheet close to the edge, again in the plane of the substrate. This third sheet is even smaller and it is barely visible in Fig. 4(IIId). The polygonal shapes of the first sheet that were observed on the horizontal substrate [17] are less present on inclined substrates.

As a curiosity specific to impacts on inclined substrates, the tiny air bubble formed below the incoming drop at the moment of impact [48, 49] also inherits some of the tangential velocity of this incoming drop. Consequently, it is advected on the substrate then possibly in the liquid sheet. It is pointed in Fig. 4(IIIc), but it is much better seen in the corresponding movie [16]. The velocity of this bubble is about 3.1 m/s and it remains approximately constant as long as the bubble can be seen. This observation is reminiscent of the absence of acceleration of fluid particles in a

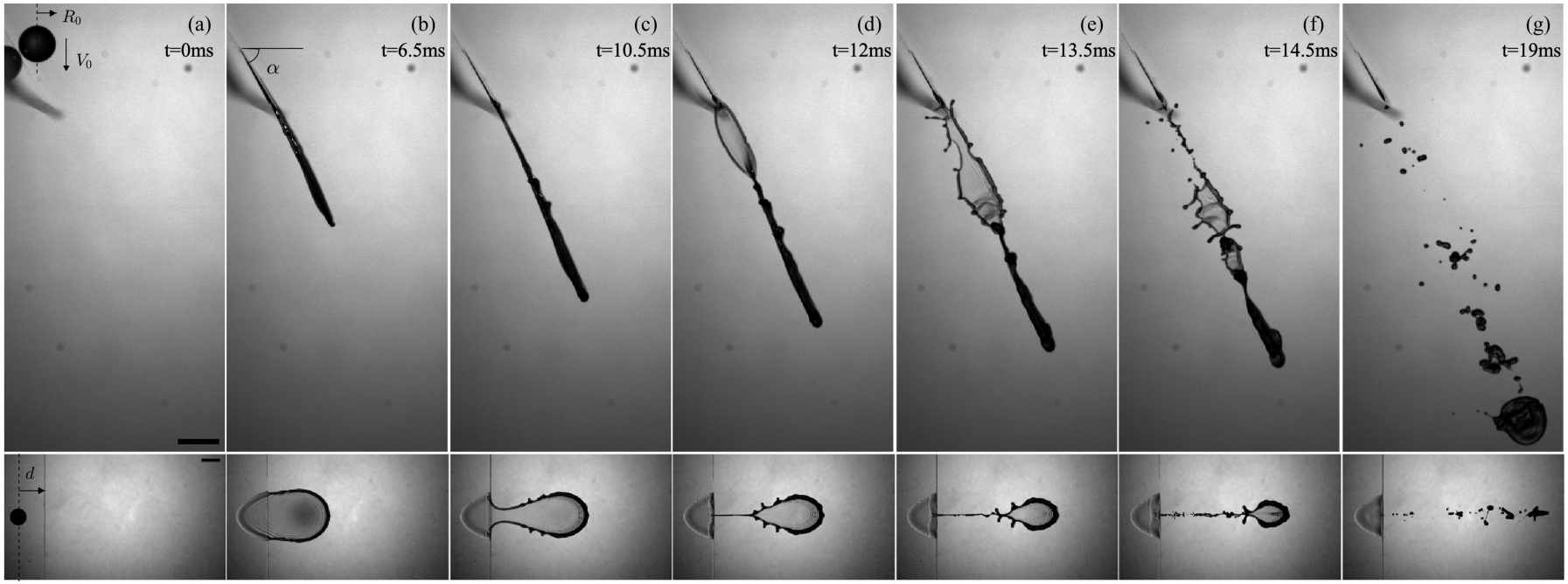

FIG. 3. Side (1st line) and top (2nd line) views of the impact of a drop of radius R_0 at speed V_0 on a substrate of inclination α, at a distance d from its edge. Dimensionless parameters are $\alpha = 60°$, $We \simeq 565$ and $d/R_0 = 2.5$. The scale bars are 5 mm and the time t from impact is indicated on each snapshot [16].

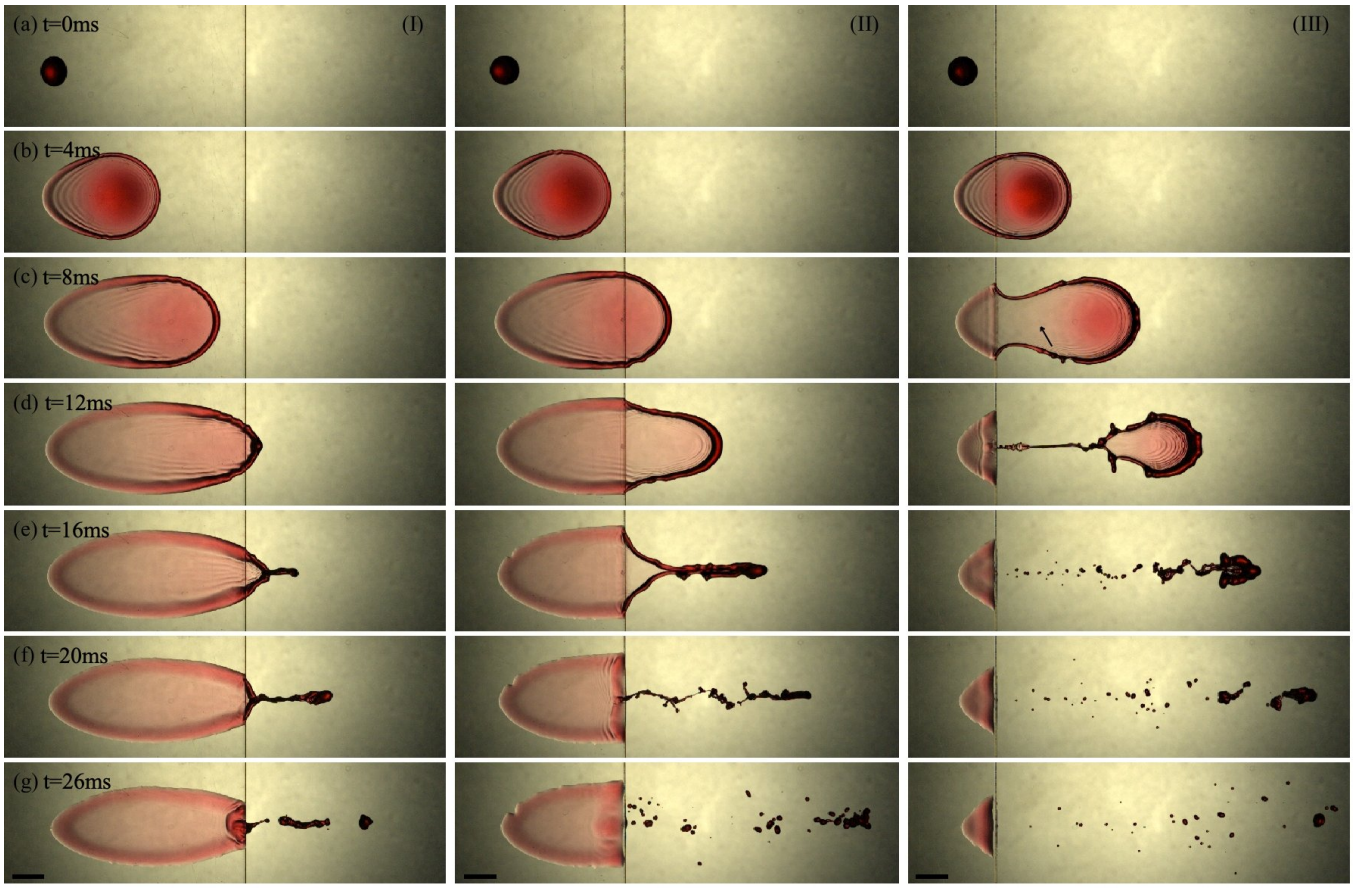

FIG. 4. Time evolution of the liquid sheet for $d/R_0 = 12$, 7.3 and 1.6 (left to right). The substrate inclination is $\alpha = 60°$ and the Weber number is $We \simeq 565$. Each column corresponds to an experiment illustrating a different sheet scenario, (I, II and III, from left to right). Snapshots in a same row are taken at the same time t from impact indicated in the leftmost snapshot [16]. Row (a) illustrates the position of the drops right before their impact, with respect to the edge. The scale bars are 5 mm. The arrow in IIIc indicates the position of a tiny air bubble trapped at early impact then advected with the sheet.

sheet formed from a drop impact on a pole [23]. During that same time, the rim expands away from the sheet (i.e., in the direction normal to the edge) with a velocity of about 5.4 m/s and minor deceleration. Therefore, the liquid in the middle of the sheet moves slower than the rim, so the flow within the sheet is likely extensional.

The scenario experienced by the sheet also depends on inclination (Fig. 5). At $We = 2115$ and $d/R_0 \in [2, 3.6]$, downward inclinations ($\alpha > 0°$) yield scenario III while the upward inclination $\alpha = -20°$ results in scenario I. A comparison of pictures taken at the same time from impact at different inclinations (Fig. 5 - column 3) reveals that the formation of corrugations during sheet expansion is delayed at large downward inclination ($\alpha = 60°$), and subsequently the first ejected droplets only appear during sheet retraction. These droplets nevertheless inherit the large speed of the rim in the direction away from the edge [16]. Numerous and much smaller droplets result from the break-up of the second liquid sheet (Fig. 5, top right snapshot). At high We and high downward inclination, the sheet bulges out of plane close to its apex, as guessed from the darker curved line close to the rim in the last snapshot of Fig. 5(a), and much better seen in the corresponding movie [16].

IV. KINEMATICS OF LIQUID SPREADING ON SOLID

The axisymmetric spreading upon vertical drop impact on a horizontal substrate was approximated in Lejeune *et al.* [17] by

$$R_s(t) \simeq R_{sM}\sqrt{\frac{t}{t_{sM}}\left(2 - \frac{t}{t_{sM}}\right)}, \tag{1}$$

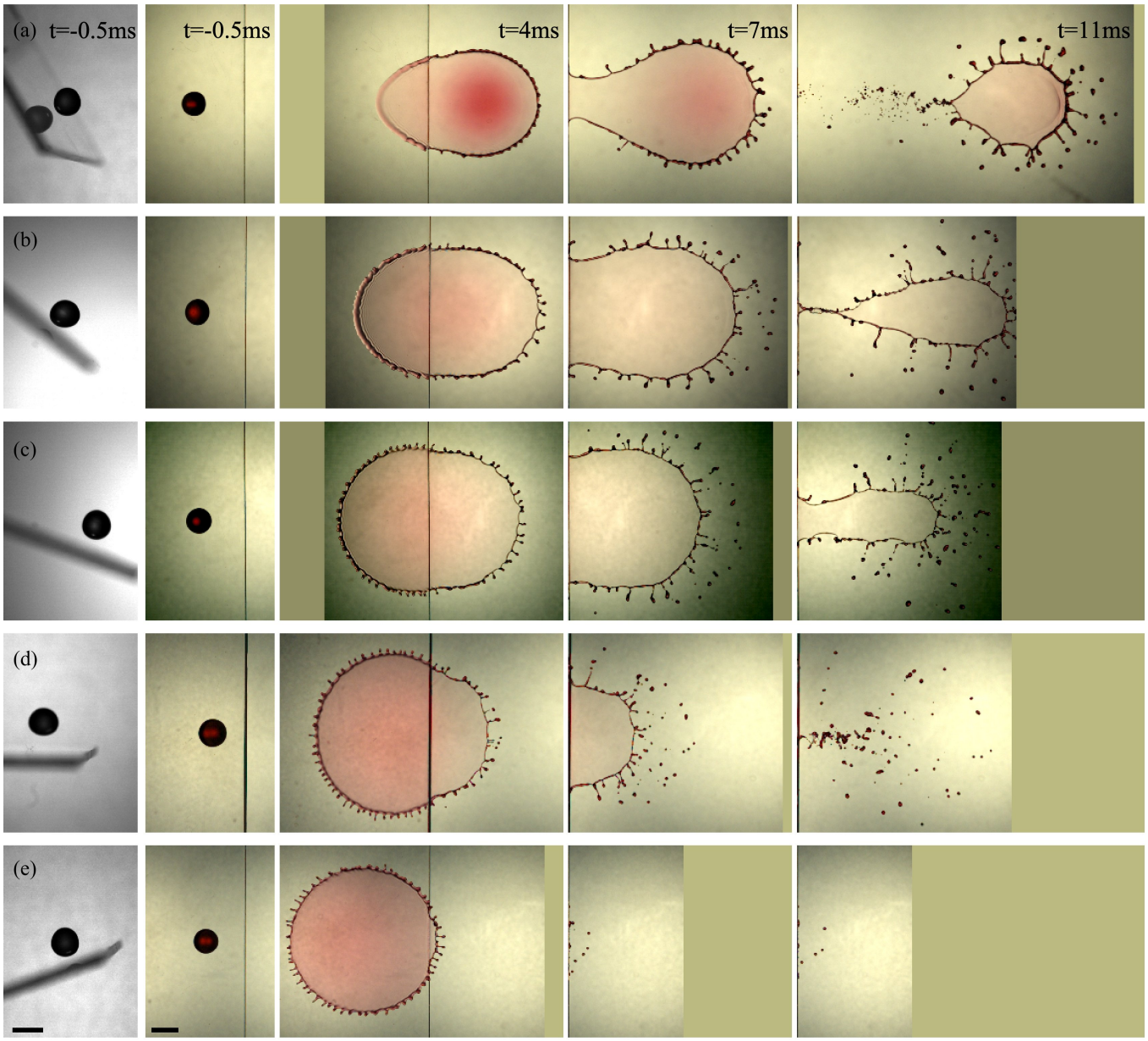

FIG. 5. Time evolution of the sheet for inclination $\alpha = 60^\circ$ (a), 40° (b), 20° (c), 0° (d) and -20° (e) with similar $d/R_0 \in [2, 3.6]$ and $We \simeq 2115$. Scenario III is observed in rows a), b) and c), while scenarios II and I are observed in rows d) and e) respectively. Snapshots in a same column are taken at the same time t from impact indicated in the top row [16]. The scale bars are 5 mm.

where R_{sM} and t_{sM} are the maximum spreading radius and the time at which it is reached, respectively. For inclined impacts, spreading is necessarily anisotropic. Its envelope, i.e. the maximum spreading in each direction, is surprisingly well approximated by an ellipse of semi-minor axis W and semi-major axis L (Fig. 6a). A systematic tracking of the ellipse formed at different α and We reveals that the impact point always coincides with the upper focus (Fig. 6b), as it was already observed for splats in plasma spray coating [50]. In a similar experiment with drops impacting on a horizontal substrate translated horizontally, Almohammadi and Amirfazli [42] showed that the shape of the spreading envelope could be reconstructed numerically by considering spreading circles of radius $R_s(t)$ and center coordinates $(V_c t, 0)$, where V_c is the speed of the substrate. Such translation of circular spreading fronts is also observed during spreading on inclined substrate, as revealed by the superposition of successive images in Fig. 6a. We therefore consider here a similar approach to rationalize the spreading envelope on an inclined substrate, this time analytically. We assume that the time evolution of the circle radius is still governed by Eq. (1). The circles then

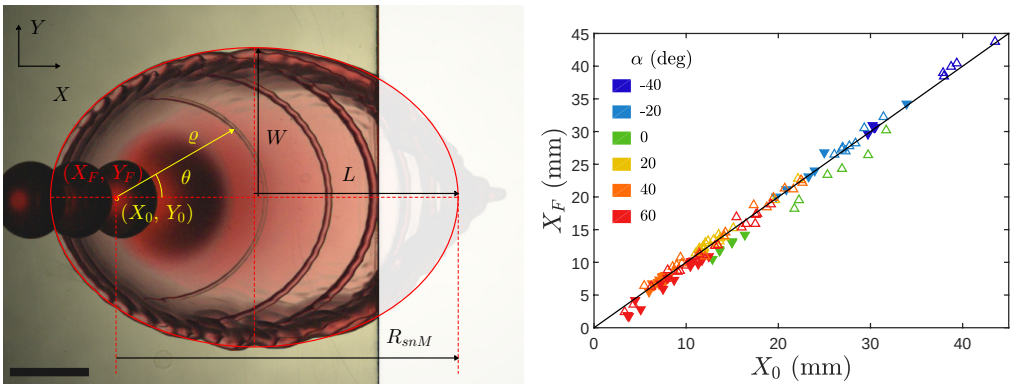

(a) (b)

FIG. 6. (a) Time superposition of the spreading following an impact at coordinates (X_0, Y_0) on an inclined substrate ($\alpha = 40°$, $We \simeq 565$, $d/R_0 \simeq 7.0$). The spreading envelope is approximated by an ellipse of minor axis W and major axis L, with one of the foci in (X_F, Y_F). Polar coordinates (ϱ, θ) are centered on the impact point. The scale bar is 5 mm. (b) Parity plot showing that X_F and X_0 are almost identical, for both $We \simeq 565$ (▼) and $We \simeq 2115$ (△) and for $\alpha \in$ [-40°, 60°] (color in legend).

satisfy

$$(\varrho\cos\theta - V_c t)^2 + \varrho^2 \sin^2\theta = R_s(t)^2 = R_{sM}^2 \frac{t}{t_{sM}}\left(2 - \frac{t}{t_{sM}}\right), \tag{2}$$

where ϱ and θ are the polar coordinates centered at the impact point (Fig. 6a). In each direction θ, the maximum spreading is achieved at the time $t_{\theta M}$ and radius ϱ_M for which

$$\left.\frac{\partial \varrho}{\partial t}\right]_\theta = 0. \tag{3}$$

Differentiating Eq. (2) according to time yields

$$\frac{t_{\theta M}}{t_{sM}} = \frac{1 + \frac{\varrho_M}{R_{sM}} v_c \cos\theta}{1 + v_c^2}, \tag{4}$$

where the dimensionless speed $v_c = V_c t_{sM}/R_{sM}$ is introduced. Substitution in Eq. (2) then results in the quadratic equation

$$\left(1 + v_c^2 \sin^2\theta\right)\frac{\varrho_M^2}{R_{sM}^2} - 2 v_c \cos\theta \frac{\varrho_M}{R_{sM}} - 1 = 0, \tag{5}$$

which positive solution is

$$\frac{\varrho_M}{R_{sM}} = \frac{v_c\cos\theta + \sqrt{1 + v_c^2}}{1 + v_c^2 \sin^2\theta} = \frac{1}{\sqrt{1 + v_c^2} - v_c \cos\theta}. \tag{6}$$

This is the polar equation of an ellipse, for which one of the foci is in $\varrho = 0$, i.e., at the impact point. The semi-minor and semi-major axes of this ellipse are given by $W = R_{sM}$ and $L = R_{sM}\sqrt{1 + v_c^2}$.

Many empirical relations and theoretical models (e.g., [38, 41, 51–54]) have been proposed to predict R_{sM}/R_0 as a function of We, Oh and the contact angle, for normal impacts on horizontal substrates. In this paper, we choose to only consider the simplest of these relations [51], namely

$$\frac{R_{sM}}{R_0} \simeq We^{1/4}. \tag{7}$$

In all the subsequent results, this expression of R_{sM} can be replaced by any other equation originating from the more involved models referenced above.

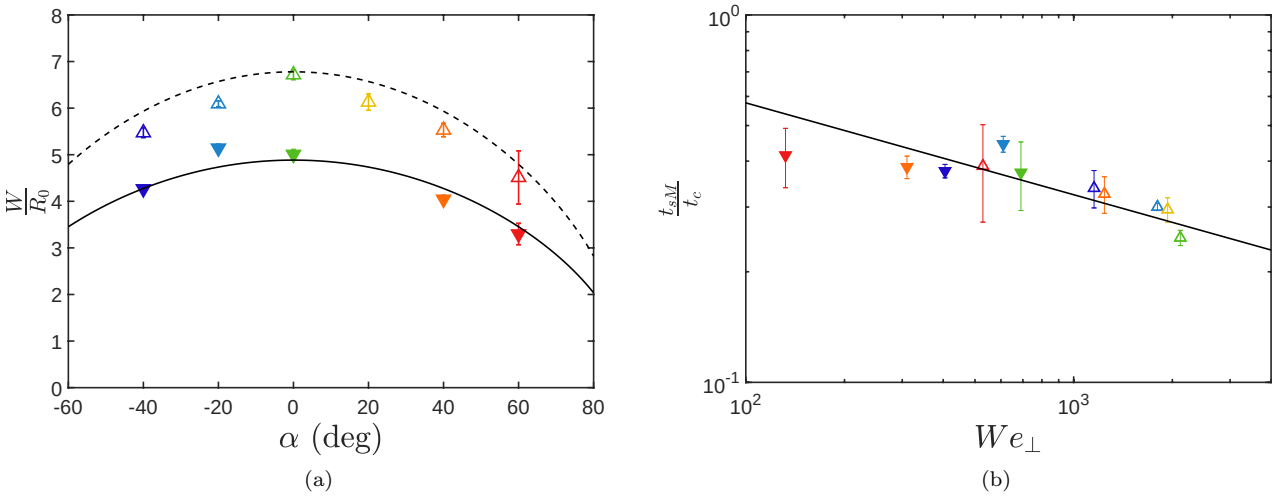

(a) (b)

FIG. 7. (a) Semi-minor axis W of the ellipse (normalized by R_0) obtained by fitting the envelope of the spreading liquid rim on the substrate as a function of α, for both $We \simeq 565$ (▼) and $We \simeq 2115$ (△). The solid (resp. dashed) lines correspond to Eq. (8) for $We = 565$ (resp. $We = 2115$). (b) Time t_{sM} (normalized by t_c) at which spreading in the direction tangent to the edge reaches its maximum value W, as a function of $We_\perp$. Symbol meaning is the same as in (a), with the color representing α. The solid line is Eq. (9) with $c_1 = 1.5$. In both (a) and (b), error bars represent the standard deviation over all experiments at a given (We, α).

Laan *et al.* [41] showed experimentally that substrate inclination could be taken into account in the prediction of R_{sM}/R_0 by replacing the Weber number We by its normal component $We_\perp = We\cos^2\alpha$ based on the normal impact speed $V_\perp = V_0\cos\alpha$. For example, Eq. 7 would become

$$\frac{R_{sM}}{R_0} \simeq We_\perp^{1/4} \simeq We^{1/4}\sqrt{\cos\alpha} \tag{8}$$

on an inclined substrate. Our measurements of $W = R_{sM}$ confirm the validity of Eq. 8 for the considered We and α [Fig. 7(a)].

In a recent theoretical work on drop spreading upon normal impact on a horizontal substrate, Gordillo *et al.* [54] showed that R_{sM} is proportional to $V_0 t_{sM}$, where the proportionality coefficient depends on the contact angle among others. This equation may also be adapted by replacing the impact speed V_0 by its normal component $V_0\cos\alpha$, namely

$$t_{sM} = c_1\frac{R_{sM}}{V_0\cos\alpha} \simeq c_1\sqrt{\frac{3}{2}}We_\perp^{-1/4}t_c, \tag{9}$$

where c_1 is a constant to be determined. The measured time of maximum spreading t_{sM} is represented as a function of $We_\perp$ in Fig. 7b. A least-squares fit of Eq.(9) on these measurements yields $c_1 \simeq 1.5$. Equation (9) captures fairly well the dependence of t_{sM} to We and α, although it strongly overpredicts the measured time for the lowest $We_\perp$ corresponding to the highest downward inclination. In sum, spreading in the horizontal direction of the inclined substrate seems to be unaffected by inclination, provided that the Weber number $We_\perp$ based on the normal impact speed is considered.

The speed V_c is measured by first approximating the liquid rim advancing on the substrate by a circular arc. We define V_c as the average translation speed of the centre of this arc. The average is considered from the time of impact to $2t_{sM}$ post impact. Figure 8 indicates that V_c is approximately proportional to $V_0\sin\alpha$, namely the tangential speed of the impacting drop. The proportionality constant is fairly close to $1/c_1 \simeq 2/3$, so the dimensionless speed is well approximated by

$$v_c = \frac{V_c t_{sM}}{R_{sM}} \simeq \tan\alpha. \tag{10}$$

The axis ratio of the ellipse is then estimated to

$$\frac{W}{L} \simeq \cos\alpha \tag{11}$$

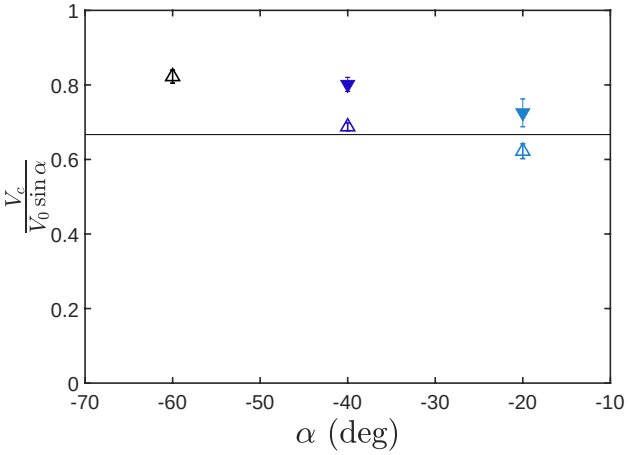

FIG. 8. Ratio between the average translation speed V_c of the center of the circular arc described by the rim as it spreads on the substrate and the tangential component of the impact speed $V_0 \sin\alpha$. Symbols correspond to different Weber numbers: $We \simeq 565$ (▼) and $We \simeq 2115$ (△). The solid horizontal line corresponds to $V_c/(V_0 \sin\alpha) = 1/c_1$.

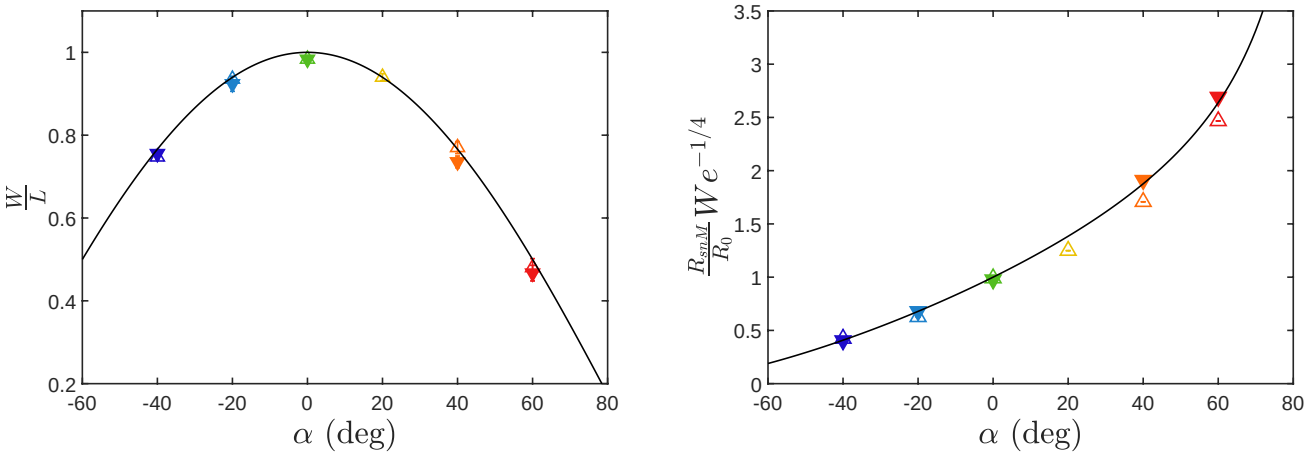

(a) (b)

FIG. 9. (a) Aspect ratio W/L of the ellipse made by the spreading envelope, and (b) maximal spreading distance R_{snM} in the direction normal to the edge, both as functions of α, for $We \simeq 565$ (▼) and $We \simeq 2115$ (△). The solid lines in (a) and (b) are Eqs. (11) and (12), respectively.

as confirmed experimentally in Fig. 9a and as already observed in the experiments of Laan *et al.* [41].

If there was no edge, the liquid spreading in the steepest direction $\theta = 0°$ could reach a distance R_{snM} from impact point given by

$$R_{snM} = \rho_M(\theta = 0°) = R_{sM} \frac{1 + \sin\alpha}{\cos\alpha} \simeq R_0 \, We^{1/4} \frac{1 + \sin\alpha}{\sqrt{\cos\alpha}}, \tag{12}$$

which is confirmed by experiments in Fig. 9b. Similarly to Lejeune *et al.* [17], a non-dimensional offset can be defined as the offset distance d from the impact point to the edge normalized by R_{snM}:

$$\delta = \frac{d}{R_{snM}} = \frac{d}{R_0} We^{-1/4} \frac{\sqrt{\cos\alpha}}{1 + \sin\alpha}. \tag{13}$$

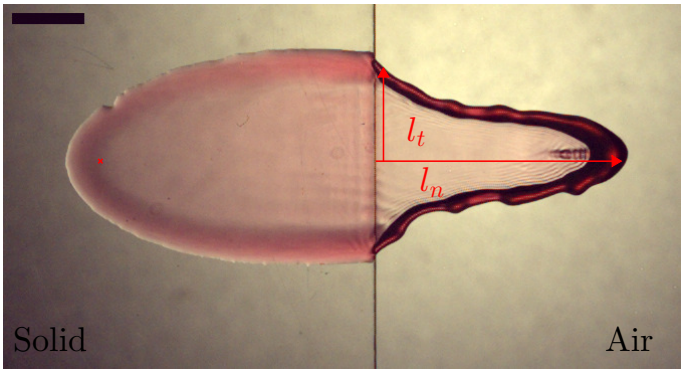

FIG. 10. Main variables l_t and l_n that characterize the liquid sheet kinematics in directions tangent and normal to the edge, respectively. The scale bar is 5 mm, and the snapshot is taken at 14.5 ms after impact, at $We \simeq 565$ and $\alpha = 60°$.

The spreading liquid reaches the edge in $(\rho, \theta) = (d, 0)$ at time $t = t_d$ which is obtained by solving Eq. (2):

$$\begin{aligned}\frac{t_d}{t_{sM}} &= \cos^2\alpha\left[1+\frac{d}{R_{sM}}\tan\alpha-\sqrt{1+2\frac{d}{R_{sM}}\tan\alpha-\frac{d^2}{R_{sM}^2}}\right]\\ &= \cos^2\alpha+\sin\alpha(1+\sin\alpha)\delta-\sqrt{\cos^2\alpha+2\sin\alpha(1+\sin\alpha)\delta-(1+\sin\alpha)^2\delta^2}\\ &= (1+\sin\alpha)\left[1-\sin\alpha(1-\delta)-\sqrt{(1-\delta)\left(\frac{1-\sin\alpha}{1+\sin\alpha}+\delta\right)}\right].\end{aligned} \tag{14}$$

V. LIQUID SHEET AND RIM KINEMATICS

The liquid sheet is formed beyond the edge of the substrate and it is delimited by a liquid rim. It is here characterized by its extension $l_n(t)$ normal to the edge (i.e., the maximum distance from the rim to the edge), and its extension $l_t(t)$ along the edge, both measured in each top-view picture (Fig. 10). Some examples of evolution of $l_n(t)$ are shown in Fig. 11a. In scenarios II and III, the normal expansion and retraction of the sheet is interrupted by a violent collapse in the direction tangent to the edge, as illustrated in Fig. 11b. Only values of $l_n(t)$ before such collapse are considered. In first approximation, the normal extension $l_n(t)$ varies quadratically with time (Fig. 11a) as it was already observed on horizontal substrates [17]:

$$l_n(t) = V_d(t-t_d) - \frac{a_n(t-t_d)^2}{2}, \tag{15}$$

where the initial speed of the rim V_d and its deceleration a_n can be fitted for each impact experiment.

The initial speed V_d of the rim in the direction normal to the edge was shown to be proportional to $V_0\sqrt{1-\delta}$ on a horizontal substrate [17]. A similar speed is observed on an inclined substrate [Fig. 12(a)] :

$$\frac{V_d}{V_0} \simeq c_2\sqrt{1-\delta}. \tag{16}$$

The coefficient c_2 is a weak function of α [Fig. 12(b)], and assuming $c_2 \simeq 1.28$ (best fitting) independent of α yields a relative error of less than 20% on V_d.

On a horizontal substrate [17], the deceleration a_n of the rim (associated to the normal extension of the sheet) was shown to be approximately proportional to $We^{1/2}$ and independent of the offset d. As seen in Fig. 13a, the independence to d (or δ) is conserved on an inclined substrate, so the deceleration a_n can be calculated for each We and α by pooling and averaging over δ. This deceleration scales as

$$a_n \simeq \frac{2R_0}{t_c^2}\,We^{1/2} f(\alpha), \tag{17}$$

where $f(\alpha)$ is a decreasing function of the substrate inclination illustrated in Fig. 13b. Gravity does not significantly contribute to the sheet acceleration. Indeed, $a_n/g \sim \sqrt{We}/Bo$ where the Bond number $Bo = \rho R_0^2 g/\sigma \simeq 0.8$. Because $We \gg 1$, $a_n/g \gg 1$ and the influence of gravity on the liquid sheet and rim dynamics can be neglected.

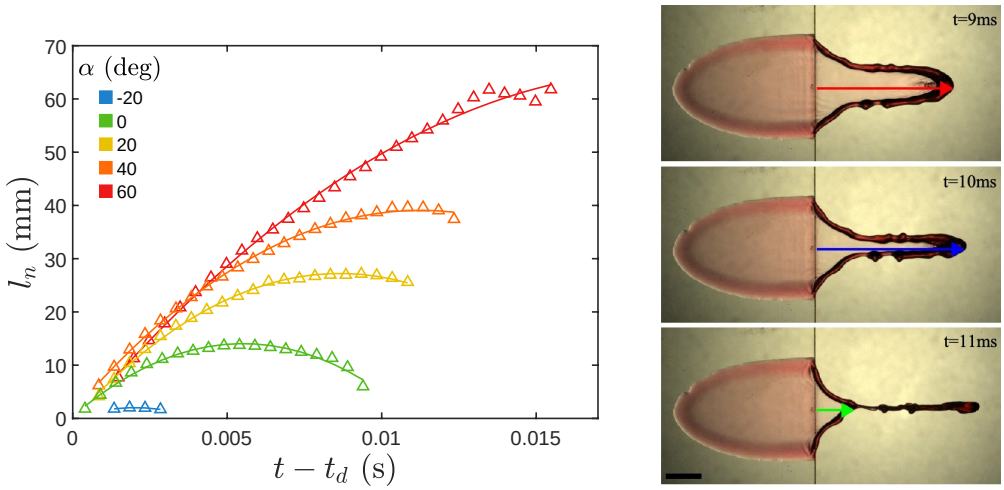

(a) (b)

FIG. 11. (a) Extension l_n of the liquid sheet normal to the edge, as a function of the time $(t - t_d)$ since the liquid reached the edge. These five experiments at $We \simeq 2115$, $\delta = 0.2$ and various α (see legend) correspond to the snapshots of Fig. 5. Symbols correspond to experimental measurements while the solid lines are the approximations by Eq. (15). (b) Snapshots of a collapse of the sheet in the direction tangent to the edge at $We \simeq 565$ and $\alpha = 60°$. The normal extension $l_n(t)$ experiences a sharp decrease. Only values of $l_n(t)$ before such collapse are considered. The scale bar is 5 mm and the time t from impact is indicated on each snapshot.

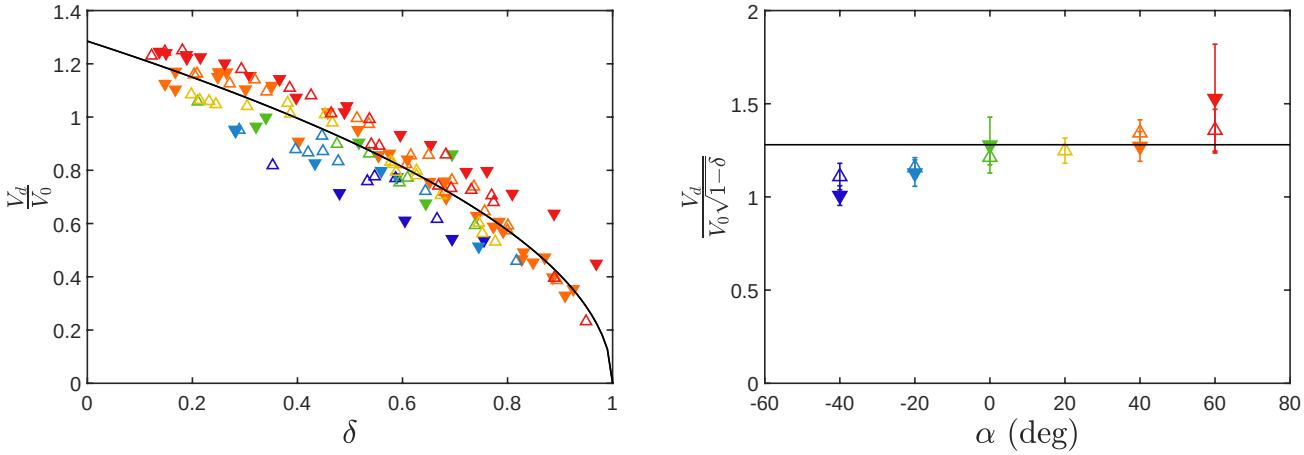

(a) (b)

FIG. 12. (a) Normalized speed V_d of the liquid rim at sheet birth, as a function of δ. (b) Same speed V_d, now normalized by $V_0\sqrt{1-\delta}$ then averaged over δ. In both (a) and (b), the solid line corresponds to Eq. (16) with $c = 1.28$. Symbols represent different Weber numbers, $We \simeq 565$ (▼) and $We \simeq 2115$ (△). Each symbol color corresponds to a different α, as given in (b).

A guess can be formulated for $f(\alpha)$, inspired by the inclination-induced stretching of the distance that the fluid can spread on the substrate in the direction normal to the edge. The stretching factor was $(1 + \sin\alpha)/\sqrt{\cos\alpha}$ (Eq. 12). We may expect that the theoretical maximum of extension of the liquid sheet $\max(l_n) = V_d^2/(2a_n)$ is stretched by the same factor. Since V_d is independent of α in first approximation, we infer

$$f(\alpha) = \frac{\sqrt{\cos\alpha}}{1 + \sin\alpha}. \tag{18}$$

This function captures very well the dependence of the rim deceleration on α (Fig. 13b).

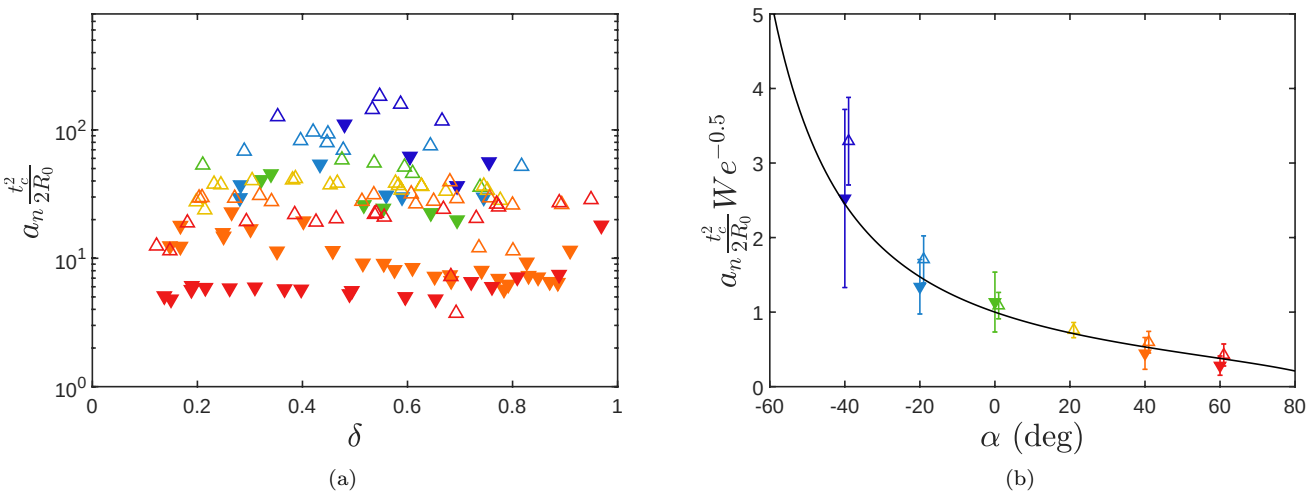

FIG. 13. (a) Normalized deceleration a_n of the rim, as a function of δ. (b) Average of $a_n t_c^2/(2R_0)$ over δ as a function of α, normalized by $We^{0.5}$. The solid line is Eq. (18). The error bar is the standard deviation over the same population. Symbols correspond to different Weber numbers, $We \simeq 565$ (▼) and $We \simeq 2115$ (△). Each symbol color corresponds to a different α, as given in (b).

The characteristic time of sheet extension normal to the edge is then given by

$$\frac{V_d}{a_n} \simeq \frac{c_2}{\sqrt{6}} \frac{\sqrt{1-\delta}}{f(\alpha)} t_c. \tag{19}$$

Remarkably, it is explicitly independent of We. It increases with increasing downward inclination α, and with decreasing offset δ. It corresponds to the time at which the rim reaches its maximum distance from the edge, although only if it is still connected to the edge at that time. We define a dimensionless time τ, which corresponds to a normalization of the time from the birth of the sheet by this characteristic time of extension normal to the edge V_d/a_n,

$$\tau = \frac{(t-t_d)a_n}{V_d}. \tag{20}$$

We proceed by rationalizing the time evolution of the rim in the vicinity of the edge, which follows that of spreading on solid during the expansion of the sheet. By contrast, dewetting on solid is decoupled from and much slower than the retraction of the liquid sheet along the edge. During sheet expansion, the extension $l_t(t)$ defined in Fig. 10 thus satisfies Eq. (2) with $l_t = \rho \sin\theta$ and $d = \rho\cos\theta$. It yields

$$\frac{l_t}{R_{sM}} = \sqrt{\frac{t}{t_{sM}}\left(2 - \frac{t}{t_{sM}}\right) - \left(\frac{d}{R_{sM}} - \frac{t}{t_{sM}}\tan\alpha\right)^2}. \tag{21}$$

By definition, $l_t = 0$ in $t = t_d$. The sheet extension along the edge reaches a maximum l_{tM} given by

$$\frac{l_{tM}}{R_{sM}} = \cos\alpha\sqrt{1 + 2\frac{d}{R_{sM}}\tan\alpha - \frac{d^2}{R_{sM}^2}} = (1+\sin\alpha)\sqrt{(1-\delta)\left[\frac{1-\sin\alpha}{1+\sin\alpha} + \delta\right]} \tag{22}$$

at a time t_{tM} from impact given by

$$\frac{t_{tM}}{t_{sM}} = \cos^2\alpha\left(1 + \frac{d}{R_{sM}}\tan\alpha\right) = (1+\sin\alpha)\left[1 - (1-\delta)\sin\alpha\right]. \tag{23}$$

Equation (22) is compared to experimental data in Fig. 14a. The agreement is reasonably good at $We \simeq 2115$, as well as at $We \simeq 565$ for downward inclinations only ($\alpha \geq 20°$). By constrast, Eq. (22) overestimates the spreading along the edge for $We \simeq 565$ and $\alpha \leq 0°$. In these conditions, the rim is significantly thicker and not perpendicular

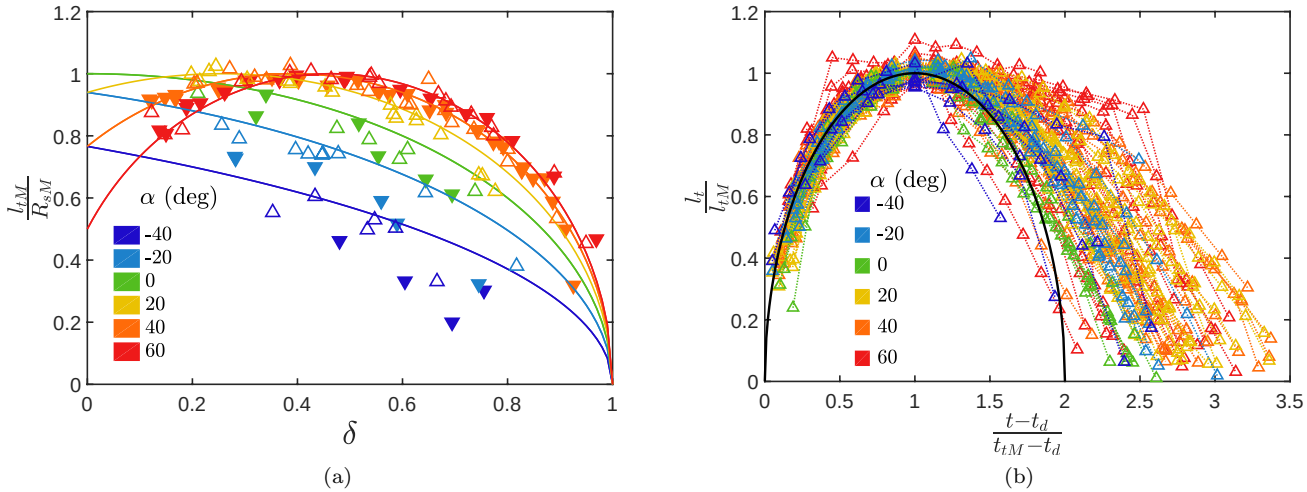

FIG. 14. (a) Maximum extension l_{tM} of the liquid sheet along the edge, normalized by the maximum spreading on solid R_{sM}, as a function of dimensionless offset δ, for $We \simeq 565$ (▼) and $We \simeq 2115$ (△), and for various α (color in legend). The solid lines correspond to Eq. (22). (b) Time evolution of the sheet extension $l_t(t)$, along the edge, normalized by its maximum value l_{tM} for $We \simeq 2115$ and various α (color in legend). Different offsets are not distinguished. The solid line represents Eq. (24).

to the edge (Fig. 4e - column 1), which then impedes the accurate measurement of l_{tM} through automated image processing.

A rescaling of this kinematics from the birth of the sheet is possible:

$$\frac{l_t}{l_{tM}} = \sqrt{\frac{t-t_d}{t_{tM}-t_d}\left(2-\frac{t-t_d}{t_{tM}-t_d}\right)}. \tag{24}$$

This rescaled extension is represented in Fig. 14b where data from the sheet expansion phase fall on the single curve of Eq. (24). However, the sheet retraction along the edge is much more scattered. This fact was already noted for impacts on a horizontal substrate [17], and it could be attributed to uncontrolled dewetting on the edge. The time t_r of collapse along the edge is usually larger than the value $t_d + 2(t_{tM} - t_d)$ that Eq. (24) would predict, which may suggest an additional dissipation mechanism. The delay in tangential collapse is more pronounced for larger α.

The competition of timescales of expansion/retraction along vs. normal to the edge can be expressed through the time ratio

$$\tau_{tM} = \frac{(t_{tM}-t_d)a_n}{V_d} = \frac{3c_1}{c_2}\,We^{-1/4}\sqrt{\frac{1-\sin\alpha}{1+\sin\alpha}+\delta} \tag{25}$$

according to Eqs. (14), (19) and (23). This ratio monotonically decreases with increasing α and increases with increasing δ. It suggests that at small α and large δ, $\tau_{tM} \gtrsim 1$ and the sheet collapses first normally to the edge, which corresponds to scenario I. On the other hand, at large α and small δ, $2\tau_{tM} \ll 1$ so the rim collapses along the edge and the sheet detaches before it starts to retract normally to the edge, which corresponds to scenario III. The correspondence between half of the normalized time of full retraction along the edge

$$\tau_r = \frac{(t_r - t_d)a_n}{V_d} \tag{26}$$

and the timescale ratio τ_{tM} is shown in Fig. 15. Since the retraction time along the edge $t_r - t_d$ is almost always larger than $2t_{tM}$, the normalized retraction time is slightly underestimated by $2\tau_{tM}$. Indeed, the measured time ratio $(t_r - t_d)a_n/(2V_d)$ appears larger than the τ_{tM} calculated from We, δ and α through Eq. (25).

The phase diagram of Fig. 16a represents the scenario experienced by the liquid sheet (described in Fig. 4), as a function of the input parameters α and d/R_0. It confirms that scenarios I, II and III are observed at high, medium and low d/R_0, respectively. However, the values of d/R_0 corresponding to the boundaries between different scenarios depend on both α and We. In Fig. 16b, the same data are plotted as a function of the variables τ_{tM} and $l_{tM}/(V_d^2/2a_n)$ representing the competition of timescale and length scale, respectively, between the sheet evolution along the edge

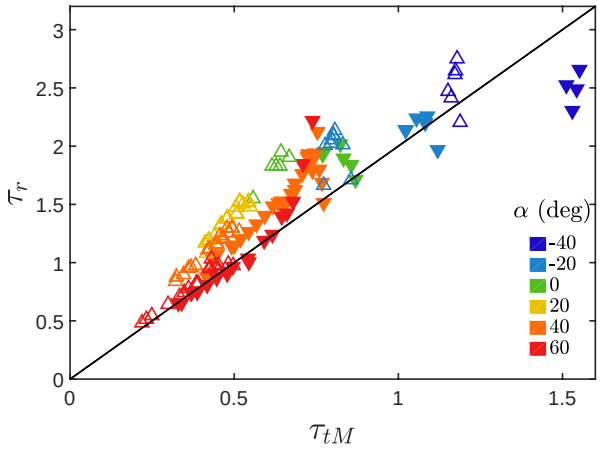

FIG. 15. Parity plot of τ_r (i.e., the measured time of full retraction along the edge $t_r - t_d$, normalized by the characteristic time of extension normal to the edge V_d/a_n) vs. the ratio τ_{tM} (i.e. the time of maximum extension along the edge, normalized similarly), for $We \simeq 565$ (▼) and $We \simeq 2115$ (△), for various α (color in legend) and δ (not distinguished). The ratio τ_{tM} is calculated from We, δ and α according to Eq. (25). Parameters V_d and a_n involved in the normalization of τ_r are also calculated, from Eqs. (16) and (17) respectively. The solid line corresponds to $\tau_r = 2\tau_{tM}$.

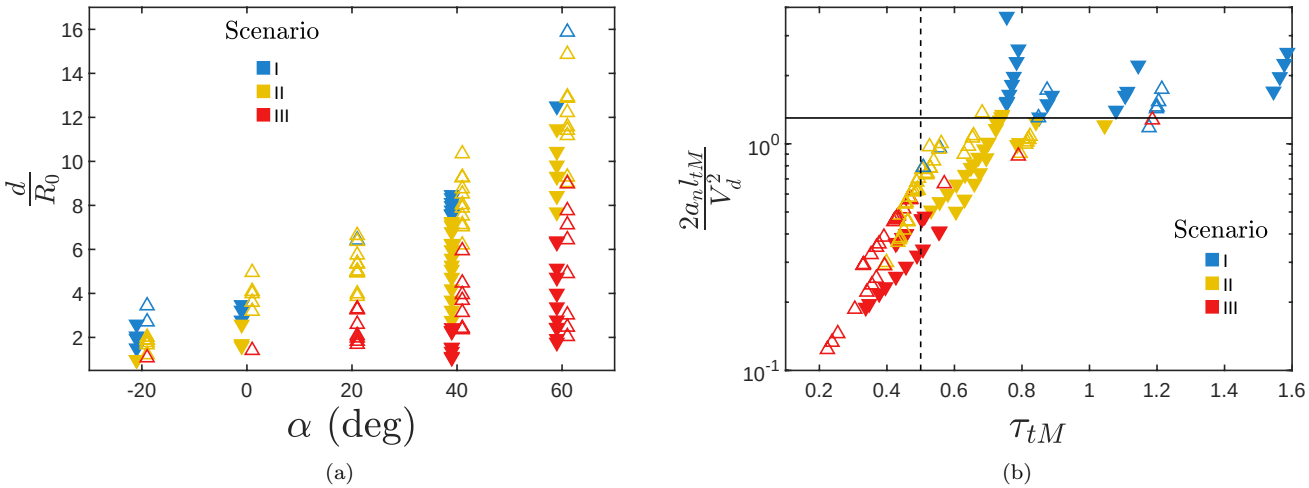

FIG. 16. Scenarios of the liquid sheet (illustrated in Fig. 4): (a) in a diagram $(\alpha, d/R_0)$, and (b) in a diagram representing the competition of timescale τ_{tM} and length scale $2a_n l_{tM}/V_d^2$. Filled symbols (resp. empty symbols) correspond to $We \simeq 565$ (resp. $We \simeq 2115$), while color indicates the scenario (cf. legend). In (b), the horizontal solid line is in $2a_n l_{tM}/V_d^2 = 1.3$. The vertical dashed line is in $\tau_{tM} = 0.5$.

and normal to the edge. The three scenarios are relatively well separated in this diagram. Scenario I is mostly found for $2a_n l_{tM}/V_d^2 > 1.3$, i.e., when the normal extension of the sheet is sufficiently small compared to the tangential extension, so the sheet can fully retract toward the edge [17]. Scenario III, which corresponds to the sheet detaching from the edge (after full retraction along the edge) while still expanding normally, is found for $\tau_{tM} < 0.5$. Scenario II is only observed for $\tau_{tM} > 0.5$ and $2a_n l_{tM}/V_d^2 < 1.3$.

VI. DROPLETS

In the previous section, the sheet kinematics was quantified based on the time evolution of the rim in directions normal to the edge and along the edge. This section is devoted to the quantitative analysis of the droplets emitted

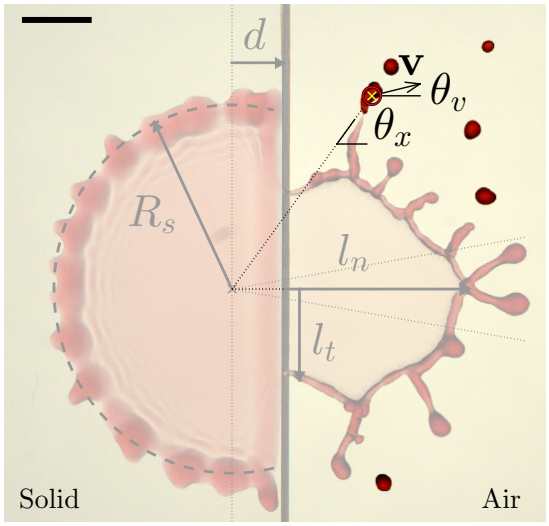

FIG. 17. Properties of ejected droplets detected by image processing: angular position of ejection (from impact point) θ_x, velocity $\mathbf{v}$, velocity direction θ_v, and radius r.

both during the sheet development and after its collapse (with a special emphasis on the former). Droplets are tracked by image processing in each experiment. Their time and position of ejection, their velocity (speed and direction) and their average radius are measured from the pictures (Fig. 17), as described in [17]. The corresponding distributions are characterized in terms of mean, minimum or maximum value, which are then related to the sheet kinematics.

Several droplet ejection mechanisms were already observed on liquid sheets emerging from the flat edge of a horizontal substrate [17]. A key differentiation can be made based on the time of ejection, which is either before or after the collapse of the sheet along the edge. Before this collapse, droplets only originate from the rim of the sheet (Fig. 18(a-b)) [20, 24]: corrugations appear on the rim because of a Plateau-like instability. As the rim decelerates, these corrugations are stretched into ligaments in response to their inertia [18, 20, 28]. The ligaments then destabilize in droplets. When the sheet collapses, i.e. when two opposite rims collide with each other, a secondary liquid sheet is formed (Fig. 3) in the perpendicular plane. This sheet also destabilizes in droplets (Fig. 18(c)) that are usually much smaller and much more scattered in direction (including out of plane), radius and speed.

The non-zero tangential speed of the impacting drop on inclined substrates allows an additional ejection mechanism that was barely observed for normal impacts on horizontal substrates [17]. At the end of spreading on the substrate (i.e., before the retraction of the sheet along the edge), the rim may still destabilize and form fingers. The size of these fingers can be considerably amplified in the direction of the tangential velocity of the impacting drop (Fig. 19a). The additional ejection mechanism is observed when the incoming drop impacts at $\delta \lesssim 1$ on a substrate inclined downward (Fig. 19b). In such conditions, the rim stops expanding soon after having reached the edge and the liquid sheet is very small. Nevertheless, the destabilization of the rim generates long fingers that break-up into droplets. These droplets inherit a small ejection speed since the rim was already almost stopped.

In the following, we separate the statistical analysis of droplets ejected before the complete retraction of the sheet along the edge ($t < t_r$) and after that full retraction ($t > t_r$).

A. Ejection before full retraction of the sheet along the edge ($t < t_r$)

1. *Direction of ejection*

Across all experiments, about 90% ($N = 4255$) of the droplets ejected at time $t < t_r$ are confined to the range $\theta_x \in [-\theta_M, \theta_M]$, $\theta_v \in [-\theta_M, \theta_M]$, where θ_M corresponds to the angle at which the wetted part of the substrate edge is seen from the impact point when it is at its maximal extension, i.e.,

$$\theta_M = \arctan \frac{l_{tM}}{d} = \arccos \left[\frac{\delta}{1 - (1-\delta)\sin\alpha} \right]. \tag{27}$$

This angle thus defines a sector of ejection and a corresponding range of velocity direction in which most droplets ejected from the rim are found. The droplet velocity at ejection is not directly correlated to the orientation of the

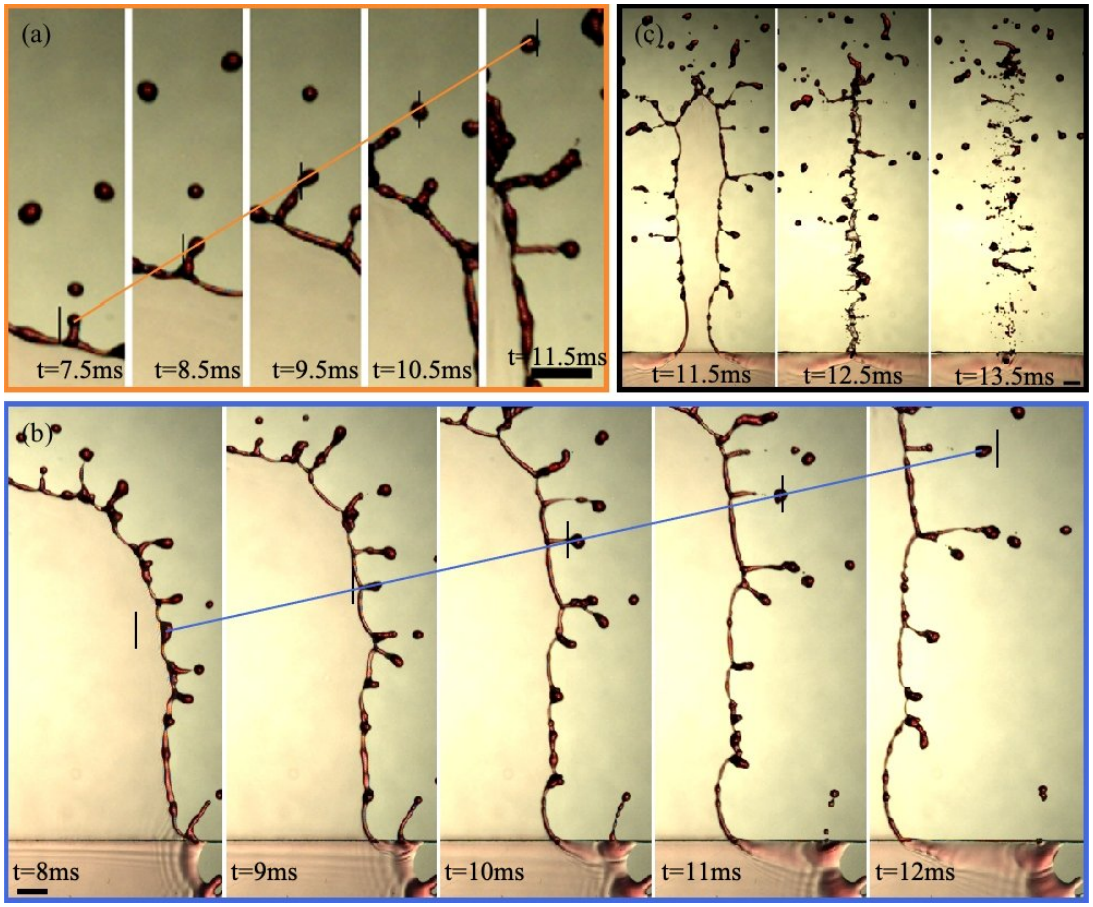

FIG. 18. Mechanisms of droplet ejection, illustrated for $\alpha = 40°$, $\delta = 0.5$ and $We \simeq 2115$. (a) Radial ejection from the rim. The ejection direction of the highlighted droplet is $\theta_v \simeq 6°$, which is here perpendicular to the rim. (b) Tangential ejection from the rim. The ejection direction of the highlighted droplet is $\theta_v \simeq 15°$, which is here much more aligned with the rim. (c) Ejections during the collapse of the sheet. In (a-c), scale bars are 2 mm and the time t from impact is indicated on each snapshot. The orange and blue solid lines join the centre of mass of the ejected droplets across frames. The vertical black lines are at fixed position, so they help visualize the left-to-right motion of the droplets.

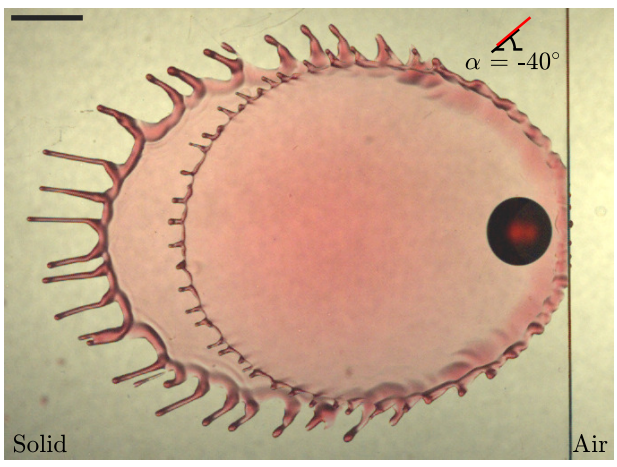

(a)

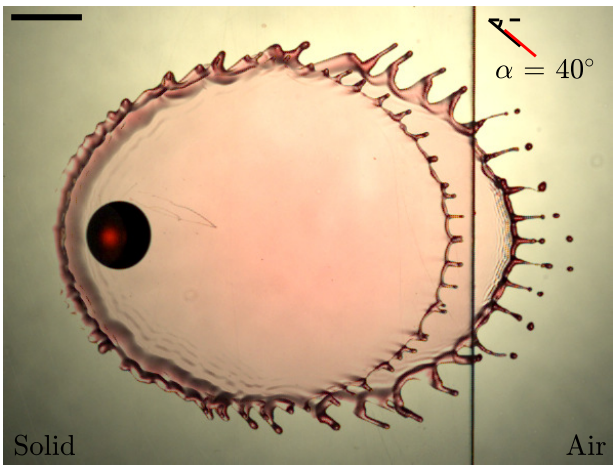

(b)

FIG. 19. Formation of fingers on inclined surfaces (a), leading to an additional droplet ejection mechanism for substrates inclined downward (b). Time superposition of a drop impacting at $We \simeq 2115$, taken at 0 ms, 4 ms and 9 ms from impact for (a) $\alpha = -40°$ and $\delta \simeq 1$; and (b) $\alpha = 40°$ and $\delta \simeq 0.9$. The scale bar is 5 mm.

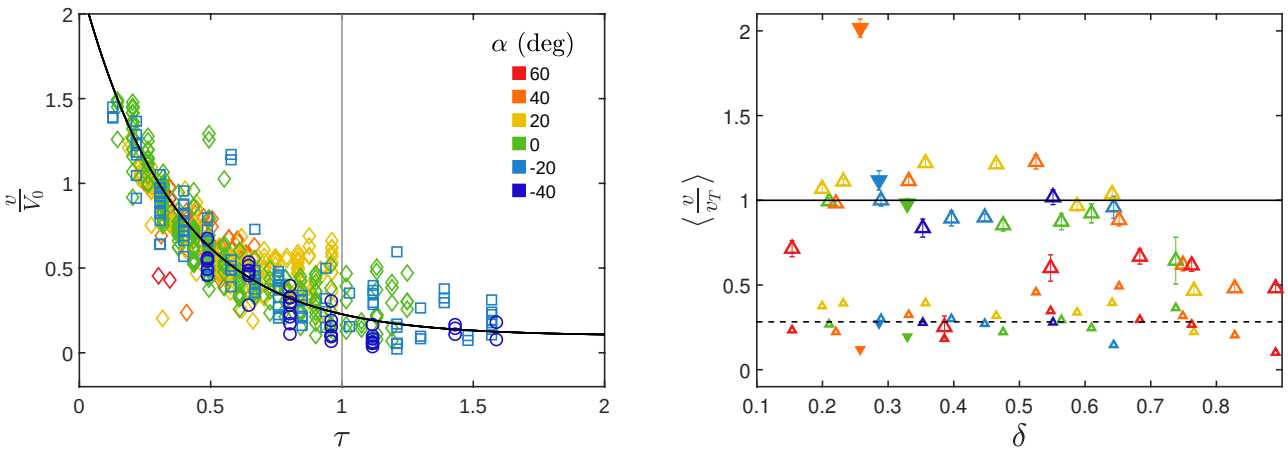

(a) (b)

FIG. 20. (a) Droplet ejection speed v, normalized by the speed V_0 of the impacting drop, as a function of the normalized time $\tau < \tau_r$. Each data point corresponds to a single ejected droplet, issued from six experiments (one per α, see color in legend) at $We \simeq 2115$ and $\delta \in [0.1, 0.3]$. The vertical gray line indicates the time of maximum sheet extension normal to the edge. The solid curve represents Eq. (28). Sheet scenarios I, II and III are represented by circles, squares and diamonds respectively. (b) Average (large symbols) and standard deviation (small symbols) of v/v_T over the sheet expansion, i.e. $\tau < \min(1, \tau_r)$, as a function of δ for $We \simeq 565$ (▼) and $We \simeq 2115$ (△) and various α [color in legend of (a)]. The solid line is $v = v_T$, according to Eq. (28). The dashed line is the average of the standard deviations (small symbols) over all (We, α, δ).

portion of rim from which it originated [17]. Indeed, the ejection velocity could be perpendicular to the rim (Fig. 18a) or more aligned with the rim (Fig. 18b).

2. *Speed*

The droplet ejection speed v normalized by the impact speed V_0 of the impacting drop is shown as a function of τ, namely the time of ejection measured from the birth of the sheet and normalized by the timescale of its normal extension V_d/a_n (Fig. 20a). The speed $v(\tau)$ is not very scattered (Fig. 20a). Its average $\langle v \rangle$ is fairly well approximated by the function $v_T(\tau)$ defined as

$$\frac{v_T}{V_0} \simeq 2.1e^{-2.8\tau} + 0.1. \tag{28}$$

This relation is similar (though with slightly different coefficients) to that proposed in Lejeune *et al.* [17] for impacts near the edge of horizontal substrates. It is purely phenomenological, and many other decreasing functions of τ could match as well this average droplet velocity. Since Eq. (28) does only depend explicitly on τ, the average speed of the ejected droplets is mostly dictated by the extension kinematics of the sheet in the direction normal to the edge. As seen in Fig. 20b, the average and standard deviation of v/v_T for droplets ejected at a time $\tau < \min(1, \tau_r)$ are respectively close to 1 and much smaller than 1, independently of We, δ and α. The average ejection speed $\langle v \rangle$ is overestimated by v_T for large δ and large α (downward). This may be due to the appearance of the additional mechanism of droplet ejection (Fig. 19) in this regime. These droplets are significantly slower, so they are expected to shift the average speed $\langle v \rangle$ down.

3. *Time of first ejection*

Some time is always needed for the rim of the sheet to decelerate and destabilize into droplets [20]. The time t_e of first droplet ejection is calculated as the quantile 1% of the ejection time of all the droplets ejected for $\tau < \tau_r$. The quantile is calculated after having pooled all droplets ejected from different impacts with the same We, δ and α. This time of first ejection is normalized by the characteristic time of normal extension of the sheet, as $\tau_e = (t_e - t_d)a_n/V_d$.

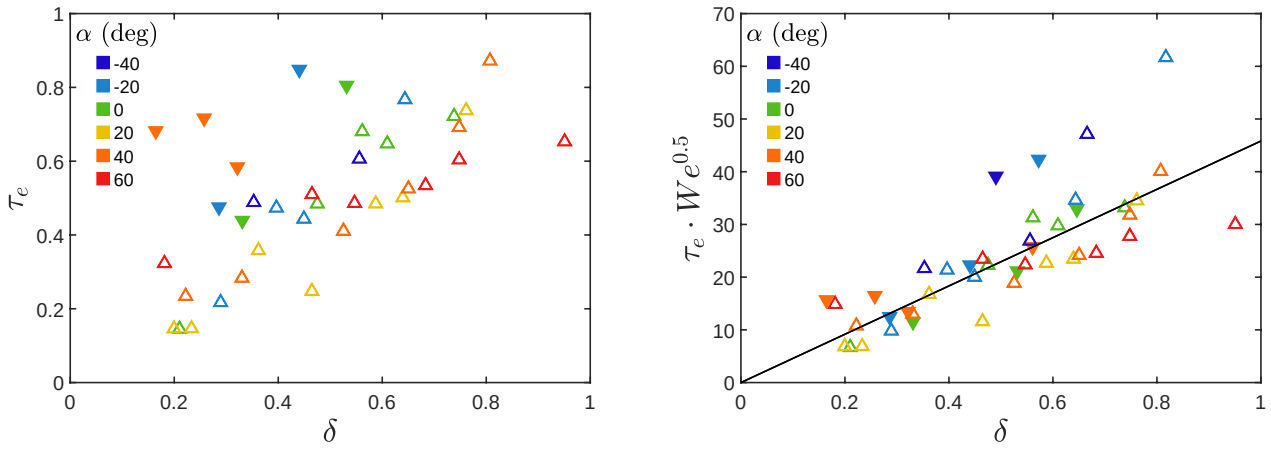

(a) (b)

FIG. 21. (a-b) Normalized time τ_e of first ejection along the rim as a function of δ, for $We \simeq 565$ (▼) and $We \simeq 2115$ (△), and for various α (color in legend). In (b), the time is further multiplied by $We^{0.5}$. The black solid line corresponds to Eq. (29).

As seen in Fig. 21, the normalized ejection time approximately satisfies

$$\tau_e \simeq c_3 \delta \, We^{-0.5}, \tag{29}$$

and it is explicitly independent of α. A best fit yields $c_3 \simeq 45$. The time of first ejection is therefore directly related to the timescale of sheet expansion in the direction normal to the edge of the substrate. In particular, for given We and δ, inclining the substrate downward decreases the sheet acceleration a_n [Eq. (17)]. This increases the timescale of the sheet V_d/a_n, which therefore postpones the ejection of the first droplets, possibly to even after the sheet collapse along the edge. This can be formalized through a comparison of τ_e and τ_r. There will be some ejection before the sheet collapses along the edge if $\tau_e < 2\tau_{tM} \lesssim \tau_r$, which, according to Eqs. (25) and (29), is the same as:

$$We > We_c \simeq \left(\frac{c_2 c_3}{6 c_1}\right)^4 \delta^4 \left(\frac{1-\sin\alpha}{1+\sin\alpha} + \delta\right)^{-2}. \tag{30}$$

The critical Weber number We_c depends on α and δ, and it is always less than $c_2 c_3/(6c_1) \simeq 1680$ since $\delta \in [0,1]$ and $\alpha \in [-\pi/2, \pi/2]$. Therefore, it is almost certain that a drop impacting at $We > 1680$ near the edge of a substrate will generate a liquid sheet that emits droplets before vanishing or detaching from this edge.

4. Droplet radius

The radius of the ejected droplets is a key property for foliar disease propagation. Indeed, not only does it condition the amount of pathogens a leaf may receive [7] but it also determines the distance travelled ballistically when combined with the ejection speed of the droplets. The radius of ejected droplets is represented as a function of time for six experiments at different inclinations in Fig. 22(a). Contrary to the ejection speed v, the radius r is scattered at all time. Nevertheless, r is clearly bounded by a maximal radius which is at least 4 times smaller than the radius R_0 of the impacting drop. This upper bound increases with the time of ejection normalized by the capillary time, according to the scaling law

$$\frac{r}{R_0} \leq c_4 \left[\frac{(t-t_d)}{t_c}\right]^{2/3}. \tag{31}$$

The constant c_4 is determined by calculating the quantile 99% of $r t_c^{2/3}/R_0/(t-t_d)^{2/3}$ for various We, α and δ [Fig. 22(b)]. This quantile is fairly independent of We, δ and α, and its average value is $c_4 \simeq 0.4$. Equation 31 can be recast as

$$t - t_d \geq c_4^{-3/2} \sqrt{\frac{4\rho r^3}{3\sigma}}. \tag{32}$$

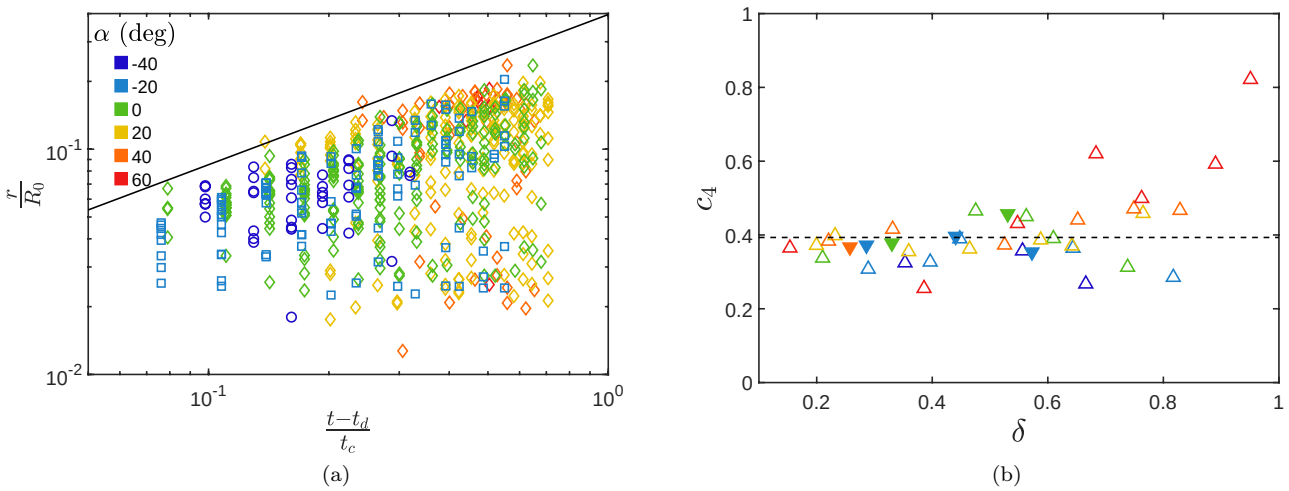

FIG. 22. (a) Radius r of the ejected droplets, normalized by the radius R_0 of the impacting drop, as a function of the time since birth of the sheet ($t - t_d$), normalized by the capillary time t_c. Each data point corresponds to a single ejected droplet, issued from six experiments (one per α, see color in legend) at $We \simeq 2115$ and $\delta \in [0.1, 0.3]$. These six experiments are the same as in Fig. 20. The solid line represents Eq. (31). (b) Coefficient c_4 of Eq. (31), calculated from the quantile 99% of $rt_c^{2/3}/R_0/(t - t_d)^{2/3}$ for each δ, α (color, as in other figures), for $We \simeq 565$ (▼) and $We \simeq 2115$ (△). The dashed line corresponds to $c_4 \simeq 0.4$.

This equation suggests that a droplet of a given size can only be ejected after some minimum time, which is of the order of four times the capillary time of this droplet. This result can be interpreted in the light of the theory developed to rationalize a similar configuration, namely the fragmentation of a liquid sheet formed by the normal impact of a drop on a pole [20, 24, 28]. Going backward in time, droplets of radius r originate from the destabilization of ligaments which radius is of the order of $2r/3$ [24]. The time to destabilize these ligaments scales as $\sqrt{\rho r^3/\sigma}$ [55, 56]. The ligaments were formed through the bulging of the rim (Plateau-like instability) and concomitant deceleration [18, 20, 28]. Nevertheless, ligaments of radius $\sim r$ are formed from a rim which radius is of the order of r [28], as observed in Fig. 5. Therefore, the time to destabilize the rim and create ligaments of radius $\sim r$ also scales as $\sqrt{\rho r^3/\sigma}$ [28]. Consequently, the minimum time from the formation of the rim to the ejection of droplets of radius r should also scale as $\sqrt{\rho r^3/\sigma}$, which Fig. 22 confirms.

Finally, we note that viscosity sets a lower bound to the size of ejected droplets. In the context of partial coalescence (i.e. coalescence of a drop with a pool of the same liquid, interrupted before completion by a pinch-off of the drop interface induced by surface tension), the inhibition of inertial liquid break-up by viscosity was observed for Ohnesorge numbers $Oh \gtrsim 0.025$ [43, 44]. It here corresponds to a minimum radius of 0.02 mm. This size is slightly below the resolution of our camera.

5. *Travelled distance*

The distributions of radius r and initial speed v of the ejected droplets are the main ingredients to input into Monte Carlo models of foliar disease dispersal [11, 12]. For example, our measurements of r and v can be used to estimate the distance travelled by the ejected droplets. In the absence of wind, these droplets fall ballistically away from the substrate. Their horizontal velocity decreases and vanishes owing to drag, while their vertical velocity converges toward their terminal speed. The maximum horizontal distance Ψ that they can travel, assuming that there is no ground to stop their fall, is called the aerodynamic wall [57]. It can be computed numerically for each droplet from its measured ejection speed v and radius r [17]. We assume here that the ejection angle is normal to the edge, i.e. $\theta_v = 0°$. The quantile 99% of Ψ, for all δ pooled together and for droplets ejected in $\tau < \tau_r$ only, is plotted as a function of α for $We \simeq 2115$ in Fig. 23. A maximum of 1.3 m is found in $\alpha = 40°$.

We can use the semi-empirical equations developed in previous sections to estimate an upper bound of the horizontal distance Ψ travelled by droplets ejected in $\tau < \tau_r$. We solve the ballistic equations again, this time with maximal radius r given by Eq. (31) and an average speed $v = v_T$ given by Eq. (28). Since both latter equations depend on the ejection time, several normalized times τ are considered in the range $\tau_e < \tau < \min(1, 2\tau_{tM})$ and only the one resulting

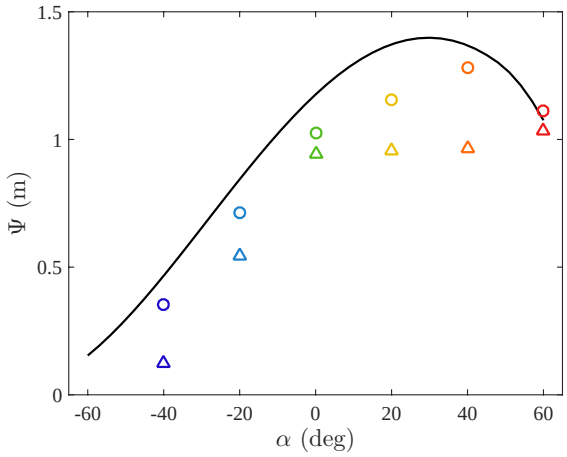

FIG. 23. Maximum distance travelled by the droplets ejected at $We \simeq 2115$, for various α, and all δ pooled together. ($\circ$) Quantile 99% of the distance travelled by droplets ejected at $\tau < \tau_r$. ($\triangle$) Quantile 99% of the distance travelled by droplets ejected at $\tau > \tau_r$. The solid line is the theoretical prediction corresponding to Fig. 24.

in the longest distance Ψ is kept. The smallest offset $\delta = 0$ is considered, as it yields the largest speed v_T and therefore potentially maximizes the travelled distance. As seen in Fig. 23, this computed upper bound is always slightly larger than the quantile 99% of the distance computed from the radius and speed of individual droplets. It peaks to 1.4 m at $\alpha = 30°$. We also calculated this upper bound for a range $We \in [67, 6700]$ close to that of raindrops [17] and for various inclinations (Fig. 24). The upper bound on Ψ increases with We and peaks at 2 m for the highest We. For a given We, the inclination α that maximizes this distance is always $\alpha \simeq 30°$. This optimum results from a trade-off: at larger α, the droplets are ejected with a velocity of larger magnitude, but with a more downward direction.

B. Ejection after full retraction of the sheet along the edge ($t > t_r$)

Many droplets are still ejected after the sheet has fully retracted along the edge, especially in sheet scenarios II and III. The ejection mechanisms of these late droplets are multiple and significantly more complex. Consequently, the droplet statistics is much more scattered for $\tau > \tau_r$ and its time evolution is less evident [17]. For example, the percentage of late droplets that still satisfy $|\theta_v| < \theta_M$ drops to 78% ($N = 12121$). There is therefore a significant number of late droplets ejected outside the sector defined by Eq.(27), and even outside the plane of the substrate (Fig. 3g). Both speed v and radius r distributions are also significantly scattered (Fig. 25). There is no apparent correlation between them, and it is possible to find late droplets that are as large and move as fast as the droplets ejected in $\tau < \tau_r$. A deeper characterization of the statistics of late droplets is left for future work. Nevertheless, we check here that these late droplets do not go over the aforementioned upper bound on travelled distance predicted from the droplet statistics in $\tau < \tau_r$. Indeed, the quantile 99% of the distance travelled by late droplets, represented in Fig. 24, is always at least 10 cm smaller than the corresponding quantile for droplets ejected in $\tau < \tau_r$.

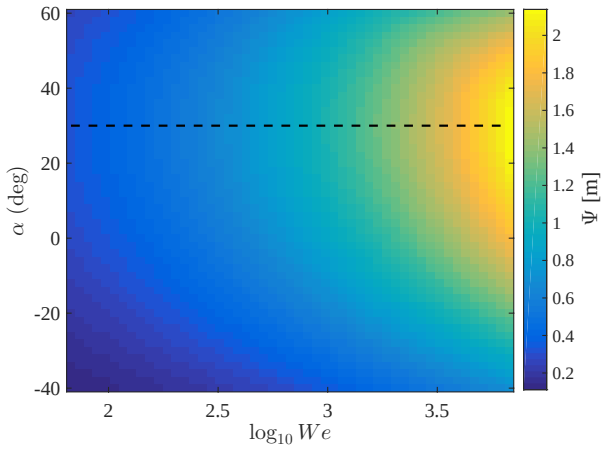

FIG. 24. Color map of the maximum horizontal distance Ψ [m] travelled by the ejected droplets, estimated theoretically for various We and α, for an incoming raindrop of radius $R_0 = 2.36$ mm with $\delta = 0$. The dashed line corresponds to the angle $\alpha = 30°$ that yields the maximum distance for a given We.

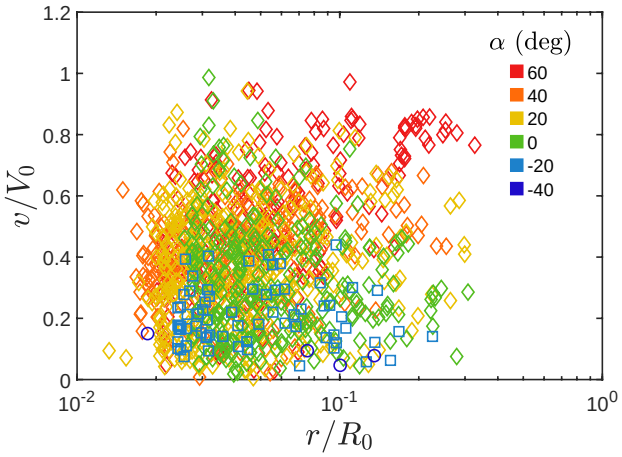

FIG. 25. Droplet ejection speed v normalized by V_0, as a function of the droplet radius r normalized by R_0, for droplets ejected after the full retraction of the sheet along the edge ($\tau > \tau_r$). Each data point corresponds to a single ejected droplet, issued from the six experiments of Fig. 20a (one per α, see color in legend) at $We \simeq 2115$ and $\delta \in [0.1, 0.3]$. Sheet scenarios I, II and III are represented by circles, squares and diamonds respectively.

VII. CONCLUSIONS

Impacts of raindrops on plant leaves are involved in the dispersal of foliar diseases responsible for important crop losses [7, 9]. However, raindrop-leaf interactions are complex and very diverse, so they are not resolved yet in current epidemiological models of crop diseases [12, 58]. Several impact scenarios were identified that were efficient at ejecting large potentially-contaminated droplets far away [14]. They share a common phenomenology: a liquid sheet surrounded by a rim grows from an edge on a substrate, then retracts and collapses. Droplets may be ejected during each phase of the sheet life. The motion of the leaf induced by the drop impact may significantly stretch this sheet and modify its break-up into droplets [8]. In this paper, we have investigated the impact of a drop next to the horizontal flat edge of an inclined planar substrate. This configuration also shares the generic phenomenological features of these observed efficient impacts, while it is significantly simpler to investigate thoroughly.

We systematically varied the Weber number We, the normalized distance to the edge δ and the substrate inclination α. We identified the dependence of each measured quantity to these three parameters, and we confirmed most of the dependences in We and δ already observed on a horizontal substrate [17]. We first demonstrated that upon impact on an inclined substrate, the rim spreads and forms an ellipse for which the upper focus is the impact point. The dimensions of this ellipse can be derived from an adaptation of the spreading laws on horizontal substrates. A liquid sheet is formed when the liquid spreads beyond the substrate edge. Both the initial speed and deceleration of the rim surrounding this sheet are proportional to the impact speed V_0, as already noticed on horizontal substrates [17] and on poles [20]. The initial speed decreases with increasing δ, but it is almost independent of α. By contrast, the deceleration of the rim depends on α but it is fairly independent of δ. Along the edge, the sheet expansion follows the spreading kinematics on the substrate, while the sheet retraction is decoupled and more stochastic. We could rationalize the competition of expansion and retraction sheet kinematics in directions normal to and along the edge, and we could relate it to the sheet scenarios observed. On a substrate inclined downward, the sheet is significantly more stretched in the direction normal to the edge, and scenario III is then observed in a much larger range of offset δ than on a horizontal substrate.

Some populations of droplets are only encountered along with specific scenarios. For example, filming synchronously from top and side allowed to identify a phenomenon typical of scenarios II and III: a second sheet perpendicular to both the substrate and its edge is formed when the rims of the first sheet collapse along the edge. It generates out-of-plane droplets that require further investigation. A new ejection mechanism specific to impacts in scenario I on substrates inclined downward has also been evidenced. We mostly focused on droplets ejected before the full retraction of the sheet along the edge. Their maximum radius and average speed both strongly depend on the time at which they are ejected: droplets emitted later are usually slower and they can be larger, as it was already evidenced on horizontal substrates [17]. The time of first ejection was also identified and it is fairly independent of inclination. We characterized the dependence of these droplet properties to ejection time and impact parameters (We, δ and α). The upper bound on the droplet radius ejected after a given time seems independent on these parameters, as it was already noticed in other configurations of liquid break-up (e.g., [56]). By contrast, both the average droplet speed and the time of earliest ejection are scaled by the characteristic time V_d/a_n of the sheet kinematics normal to the edge. This dependence of the droplet speed to the sheet kinematics was already noticed and rationalized for the simpler configuration of liquid sheets originating from the axisymmetric impact of a drop onto a pole [24]. The maximum horizontal distance travelled by the ejected droplets was calculated from their size and ejection speed. An upper bound could be estimated for all the droplets emitted by an impact at given We and α. This bound increases with We, and it is always maximal for a substrate inclined at 30° downward, independently of We.

This work has shown that substrate inclination has a major quantitative influence on the liquid sheet formed upon impact of a drop next to the substrate edge. It also confirmed that the size and speed of the droplets ejected from the rim of this sheet are directly inherited from the kinematics of this latter. Therefore, studying sheet kinematics is a prerequisite to any future investigation of droplet dispersal in more complicated and realistic impact scenarios. A first step would be to check that the observed independence of the initial speed of the rim V_d to the substrate inclination α and of the rim deceleration a_n to the dimensionless offset δ may actually be also observed similarly in more complicated impact configurations.

ACKNOWLEDGMENTS

This work was supported by the FRIA/FNRS grant FC18103.

[1] E. Villermaux, "Fragmentation," Annual Review of Fluid Mechanics **39**, 419–446 (2007).
[2] P. I. A. Kinnell, "Raindrop-impact-induced erosion processes and prediction: a review," Hydrol. Process. **19**, 2815–2844 (2005).
[3] Y. S. Joung and C. R. Buie, "Aerosol generation by raindrop impact on soil," Nat. Comm. **6**, 6083 (2015).
[4] B. Blocken, D. Derome, and J. Carmeliet, "Rainwater runoff from building facades: a review," Building and Environment **60**, 339–361 (2013).
[5] G. J. Amador, Y. Yamada, M. McCurley, and D. L. Hu, "Splash-cup plants accelerate raindrops to disperse seeds," J. R. Soc. Interface **10**, 20120880 (2012).
[6] D. J. Furbish, K. K. Hammer, M. Schmeeckle, M. N. Borosund, and S. M. Mudd, "Rain splash of dry sand revealed by high-speed imaging and sticky paper splash targets," Journal of Geophysical Research: Earth Surface **112**, 1–9 (2007).
[7] B. D. L. Fitt, H. A. McCartney, and P. J. Walklate, "The role of rain in dispersal of pathogen inoculum," Annu. Rev. Phytopathol. **27**, 241–270 (1989).
[8] T. Gilet and L. Bourouiba, "Fluid fragmentation shapes rain-induced foliar disease transmission," Journal of the Royal Society Interface **12**, 20141092 (2015).
[9] E.-C. Oerke, "Crop losses to pests," J. Agric. Sci. **144**, 31–43 (2006).
[10] A. Calonnec, J.-B. Burie, M. Langlais, S. Guyader, S. Saint-Jean, I. Sache, and B. Tivoli, "Impacts of plant growth and architecture on pathogen processes and their consequences for epidemic behaviour," European Journal of Plant Pathology **135**, 479–497 (2013).
[11] C. Gigot, C. De Vallavieille-Pope, L. Huber, and S. Saint-Jean, "Using virtual 3-d plant architecture to assess fungal pathogen splash dispersal in heterogeneous canopies: A case study with cultivar mixtures and a non-specialized disease causal agent," Annals of Botany **114**, 863–875 (2014).
[12] T. Vidal, P. Lusley, M. Leconte, C. De Vallavieille-Pope, L. Huber, and S. Saint-Jean, "Cultivar architecture modulates spore dispersal by rain splash: A new perspective to reduce disease progression in cultivar mixtures," PLoS ONE **12**, e0187788 (2017).
[13] I. Pertot, T. Caffi, V. Rossi, L. Mugnai, C. Hoffmann, M. S. Grando, C. Gary, D. Lafond, C. Duso, D. Thiery, V. Mazzoni, and G. Anfora, "A critical review of plant protection tools for reducing pesticide use on grapevine and new perspectives for the implementation of ipm in viticulture," Crop Protection **97**, 70–84 (2017).
[14] T. Gilet and L. Bourouiba, "Rain-induced ejection of pathogens from leaves: Revisiting the hypothesis of splash-on-film using high-speed visualization," Integr. Comp. Biol. **54**, 974–984 (2014).
[15] Y. Wang and L. Bourouiba, "Non-isolated drop impact on surfaces," J. Fluid Mech. **835**, 24–44 (2018).
[16] See Supplemental Material at [URL will be inserted by publisher] for the corresponding movies.
[17] S. Lejeune, T. Gilet, and L. Bourouiba, "Edge effect: Liquid sheet and droplets formed by drop impact close to an edge," Phys. Rev. Fluids **3**, 083601 (2018).
[18] A. Rozhkov, B. Prunet-Foch, and M. Vignes-Adler, "Impact of water drops on small targets," Phys. Fluids **14**, 3485–3501 (2002).
[19] A. Rozhkov, B. Prunet-Foch, and M. Vignes-Adler, "Dynamics of a liquid lamella resulting from the impact of a water drop on a small target," Proceedings of the Royal Society A: Mathematical, Physical and Engineering Sciences **460**, 2681–2704 (2004).
[20] E. Villermaux and B. Bossa, "Drop fragmentation on impact," J. Fluid Mech. **668**, 412–435 (2011).
[21] C. Vernay, L. Ramos, and C. Ligoure, "Free radially expanding liquid sheet in air: Time-and space-resolved measurement of the thickness field," Journal of Fluid Mechanics **764**, 428–444 (2015).
[22] S. Arora, C. Ligoure, and L. Ramos, "Interplay between viscosity and elasticity in freely expanding liquid sheets," Physical Review Fluids **1**, 083302 (2016).
[23] Y. Wang and L. Bourouiba, "Drop impact on small surfaces: Thickness and velocity profiles of the expanding sheet in the air," Journal of Fluid Mechanics **814**, 510–534 (2017).
[24] Y. Wang and L. Bourouiba, "Unsteady sheet fragmentation: droplet sizes," J. Fluid Mech. **848**, 946–967 (2018).
[25] G. Liang, Y. Guo, Y. Yang, and S. Shen, "Liquid sheet behaviors during a drop impact on wetted cylindrical surfaces," Int. Comm. Heat Mass Transfer **54**, 67–74 (2014).
[26] Y. Liu, M. Andrew, J. Li, J. M. Yeomans, and Z. Wang, "Symmetry breaking in drop bouncing on curved surfaces," Nature Communications **6**, 10034 (2015).
[27] M. Arogeti, D. Sher, and E. Sher, "Drop impact on a small target with an inclined plane," Exp. Therm. Fluid Sci. **99**, 140–148 (2018).
[28] Y. Wang, R. Dandekar, N. Bustos, S Poulain, and L. Bourouiba, "Universal rim thickness in unsteady sheet fragmentation," Phys. Rev. Lett. **120**, 204503 (2018).
[29] X. Zou, M. Mõttus, P. Tammeorg, C. L. Torres, T. Takala, J. Pisek, P. Mäkelä, F.L. Stoddard, and P. Pellikka, "Photographic measurement of leaf angles in field crops," Agricultural and Forest Meteorology **184**, 137–146 (2014).

[30] L. Tadrist, M. Saudreau, and E. de Langre, "Wind and gravity mechanical effects on leaf inclination angles," J. Theor. Biol. **341**, 9–16 (2014).

[31] L. Tadrist, K. Julio, M. Saudreau, and E. de Langre, "Leaf flutter by torsional galloping: Experiments and model," J. Fluids Struct. **56**, 1–10 (2015).

[32] D. Soto, A. B. De Larivière, X. Boutillon, C. Clanet, and D. Quéré, "The force of impacting rain," Soft Matter **10**, 4929–4934 (2014).

[33] S. Gart, J. E. Mates, C. M. Megaridis, and S. Jung, "Droplet impacting a cantilever: a leaf-raindrop system," Phys. Rev. Applied **3**, 044019 (2015).

[34] Š. Šikalo, C. Tropea, and E. N. Gani, "Impact of droplets onto inclined surfaces," Journal of Colloid and Interface Science **286**, 661–669 (2005).

[35] T. Gilet and J. W. M. Bush, "Droplets bouncing on a wet, inclined surface," Phys. Fluids **24**, 122103 (2012).

[36] C. Antonini, F. Villa, and M. Marengo, "Oblique impacts of water drops onto hydrophobic and superhydrophobic surfaces: Outcomes, timing, and rebound maps," Experiments in Fluids **55**, 1713 (2014).

[37] Y. H. Yeong, J. Burton, E. Loth, and I. S. Bayer, "Drop impact and rebound dynamics on an inclined superhydrophobic surface," Langmuir **30**, 12027–12038 (2014).

[38] D. H. Kwon, H. K. Huh, and S. J. Lee, "Wettability and impact dynamics of water droplets on rice (oryza sativa l.) leaves," Exp. Fluids **55**, 1691 (2014).

[39] R. Zhang, P. Hao, and F. He, "Drop impact on oblique superhydrophobic surfaces with two-tier roughness," Langmuir **33**, 3556–3567 (2017).

[40] J. C. Bird, S. H. Tsai, and H. A. Stone, "Inclined to splash: Triggering and inhibiting a splash with tangential velocity," New Journal of Physics **11**, 063017 (2009).

[41] N. Laan, K. G. de Bruin, D. Bartolo, C. Josserand, and D. Bonn, "Maximum diameter of impacting liquid droplets," Phys. Rev. Applied **2**, 044018 (2014).

[42] H. Almohammadi and A. Amirfazli, "Asymmetric spreading of a drop upon impact onto a surface," Langmuir **33**, 5957–5964 (2017).

[43] F. Blanchette and T. P. Bigioni, "Partial coalescence of drops at liquid interfaces," Nat. Phys. **2**, 254–257 (2006).

[44] T. Gilet, K. Mulleners, J.-P. Lecomte, N. Vandewalle, and S. Dorbolo, "Critical parameters for the partial coalescence of a droplet," Phys. Rev. E **75**, 036303 (2007).

[45] J. W. M. Bush and A. E. Hasha, "On the collision of laminar jets: fluid chains and fishbones," J. Fluid Mech. **511**, 285–310 (2004).

[46] N. Bremond and E. Villermaux, "Atomization by jet impact," J. Fluid Mech. **549**, 273–306 (2006).

[47] C. Adam, "Fundamental studies of bloodstain formation and characteristics," Forensic Science International **219**, 76–87 (2012).

[48] S. Chandra and C.T. Avedisian, "On the collision of a droplet with a solid surface," Proc. R. Soc. A **432**, 13–41 (1991).

[49] S. Thoroddsen, T. G. Etoh, K. Takehara, N. Ootsuka, and Y. Hatsuki, "The air bubble entrapped under a drop impacting on a solid surface," J. Fluid Mech. **545**, 203–212 (2005).

[50] C. W. Kang and H. W. Ng, "Splat morphology and spreading behavior due to oblique impact of droplets onto substrates in plasma spray coating process," Surface and Coatings Technology **200**, 5462–5477 (2006).

[51] C. Clanet, C. Beguin, D. Richard, and D. Quéré, "Maximal deformation of an impacting drop," J. Fluid Mech. **517**, 199–208 (2004).

[52] I. V. Roisman, E. Berberović, and C. Tropea, "Inertia dominated drop collisions. i. on the universal flow in the lamella," Physics of Fluids **21**, 052103 (2009).

[53] J. Eggers, M. A. Fontelos, C. Josserand, and S. Zaleski, "Drop dynamics after impact on a solid wall: Theory and simulations," Physics of Fluids **22**, 062101 (2010).

[54] J. M. Gordillo, G. Riboux, and E. S. Quintero, "A theory on the spreading of impacting droplets," J. Fluid Mech. **866**, 298–315 (2019).

[55] P. Marmottant and E. Villermaux, "Fragmentation of stretched liquid ligaments," Phys. Fluids **16**, 2732 (2004).

[56] J. M. Gordillo and S. Gekle, "Generation and breakup of worthingon jets after cavity collapse. part 2. tip breakup of stretched jets," J. Fluid Mech. **663**, 331–346 (2010).

[57] C. Cohen, B. Darbois-Texier, G. Dupeux, E. Brunel, D. Qur, and C. Clanet, "The aerodynamic wall," Proceedings of the Royal Society A: Mathematical, Physical and Engineering Sciences **470**, 20130497 (2013), cited By 9.

[58] S. Saint-Jean, M. Chelle, and L. Huber, "Modelling water transfer by rain-splash in a 3d canopy using monte carlo integration," Agricultural and Forest Meteorology **121**, 183–196 (2004).